Chapter 3

Synthesis of Adsorbents for the Removal of Uranium from Aqueous Solution

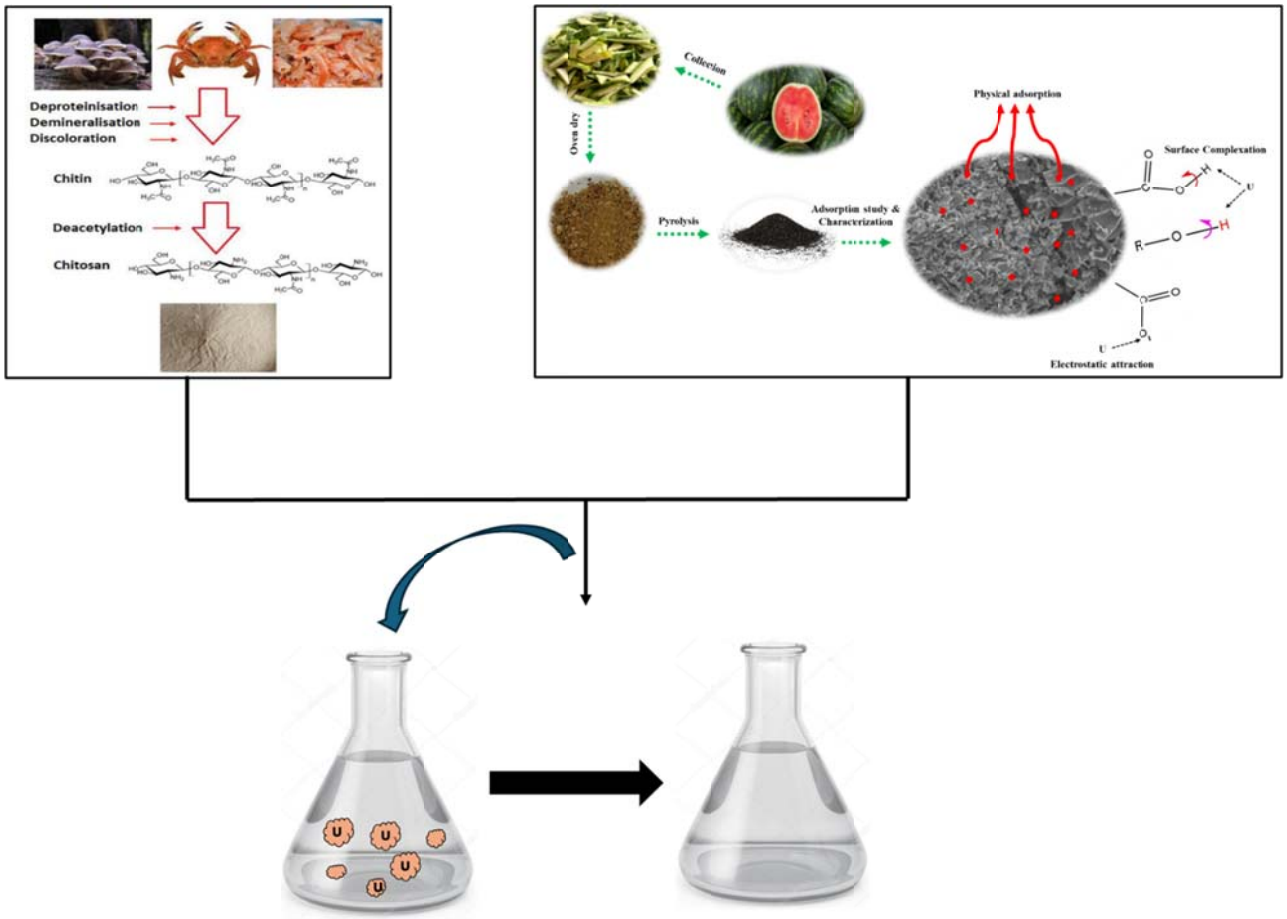

3.1. Introduction

In the last few decades, a large number of adsorbents have been developed to recover uranium from water resources, such as clay minerals, modified palm shell powder, activated carbon, graphene oxides, chelating resins, and magnetic metal oxides, etc. (Abney et al., 2017; Kushwaha and Sudhakar, 2013; Liu et al., 2019; Wang et al., 2019). In the past few decades, polymer-based materials have been exhaustively studied as efficient adsorbents for uranium because such materials can be modified with functional groups and designed to have unique properties that show remarkable characteristics including large surface area, increased porosity, and multi-functionality (Pan et al., 2009). Due to its cationic behavior in acidic solution, chitosan, one of the well-known biopolymers, has unique features that differentiates it from other polysaccharides. Raw biopolymers have low porosity and persistent crystallinity, which restrict access to internal reactive groups and complicate hydration. To improvise the performance of the adsorbent, usually chelating substances are used which overcome the above-mentioned short comings. Functionalization or derivatization further enhanced the adsorption and chelating abilities of chitosan (Kyzas and Bikiaris, 2015). A variety of ligands, including barbituric acid, oxine, glycine, iminodiacetic acid (IDA), ethylene glycol bis(2-aminoethylether)-N,N,N',N'-tetraacetic acid (EGTA), ethylenediaminetetraacetic acid (EDTA), and diethylenetriaminepentaacetic acid (DTPA), etc., have been used to modify chitosan for the effective removal of different elements and remediation of wastewater (Hamza et al., 2019; Kushwaha and Sudhakar, 2011; Repo et al., 2010). For the uptake of uranium from aqueous solution, Suresh Kumar and his colleagues synthesized crosslinked chitosan with sodium tripolyphosphate. (Sureshkumar et al., 2010). For the adsorption of Co(II) from water in the presence of EDTA and other interfering species, Evelina Repo et al. utilised EDTA-modified chitosan(Repo et al., 2013). Additionally, they used modified chitosan-silica hybrids with EDTA as adsorbents to remove the ions of cobalt, nickel, cadmium, and lead from aqueous solutions (Repo et al., 2011b). Researchers have employed DTPA as well as silica gel modified chitosan to remove cobalt and chromium from aqueous solutions (Bhatt et al., 2015; Repo et al., 2011a). However, DTPA-modified chitosan's ability to adsorb uranium from water-based systems has not been explored till date.

In addition to biopolymers, biochar is also an alternative for remediating water containing radioactive elements, heavy metals, and other contaminants. Over the past few years, biochar, an emerging carbon-rich substance created from inexpensive biomass waste through

simple pyrolysis, has drawn significant attention as an effective adsorbent to remove water pollutants (Han et al., 2017; Jin et al., 2018; Luo et al., 2021). In addition to eliminating water contaminants, biochar is used in other sectors, such as energy production (Chi et al., 2021; Kant Bhatia et al., 2021), soil amendment (Adhikari et al., 2022; Wu et al., 2012) and others (Hu et al., 2020; Kamali et al., 2022) due to the presence of mineral content, large specific surface area, rich porous structure, and availability of surface functional groups. Biochar is synthesized from a variety of biomass, including straw, maize cobs, animal manure, wastewater sludge, fruit wastes, and vegetable wastes, etc. (Albayari et al., 2021; Gopinath et al., 2021; Liao et al., 2022a; Lingamdinne et al., 2022).

Furthermore, using these wastes to make biochar lessens the global ecological burden, reduces waste volume, and promotes the mass manufacturing of low-cost, long-lasting adsorbents for water and wastewater treatment, as well as uranium recovery from seawater. The biochar synthesis conditions, and treatment parameters are the major contributors to the advantages of such adsorbents. In previous studies many approaches to improve the efficiency and functional groups of biochar have been applied (Lingamdinne et al., 2022; Wang et al., 2021). Furthermore, modified biochars require more chemicals and energy to improve efficiency, as well as additional functional groups on the surface. Literature shows that many modified biochar and high-temperature pyrolyzed biochar from organic waste have been used to extract elements such as uranium from aqueous solutions (Lingamdinne et al., 2022; Morsy, 2015; Wang et al., 2021; Xu et al., 2020). Because of this, it's necessary to search for less expensive biochar substitutes to remove uranium from waste and marine water; this work additionally depends on energy management. Watermelon rind, on the other hand, is a plentiful fruit waste product, yielding 117 million tonnes worldwide, but its biochar has not received as much attention as it could for uranium adsorption. Watermelon peels are rich in phenolic compounds, fatty acids, and carbohydrates. Melon peels' carbohydrate content mostly consists of cellulose, hemicelluloses, and pectin, with the main monosaccharides being glucose, xylose, and galactose. This makes watermelon peels a good substitute for producing biochar (Sadhu et al., 2021). Keeping these things in mind, the viability of producing low-cost, unmodified biochar at low temperatures from watermelon peels, an agricultural by-product, and chitosan DTPA were investigated for the adsorption of uranium from aqueous solutions.

3.2.Characterisation of the prepared adsorbents

An ALPHA-T IR (Bruker) spectrometer was used to carry out the Fourier Transform Infrared (FTIR) measurements which was used to detect the presence of functional groups present on the surface of the synthesized adsorbents. Under a nitrogen environment, thermogravimetric analysis (TGA) was performed using Exstar 6000 TG-DTA-6300 thermal analyser. The porosity of the adsorbents has been determined via BET analysis using Micromeritics ASAP 2010. The morphological properties of the surface of the adsorbents for the pre and post adsorption was examined using SU1510 scanning electron microscopy (SEM). EDX analysis (JSM-7600F) was utilized to determine the material's elemental composition both before and after uranium adsorption. To determine the crystal lattice parameters XRD measurement of samples were performed using Bruker D8 Advance A25. In addition to these methods, XPS (PHI 5000 VersaProbe III model) was carried out for speciation and to elucidate the underlaying mechanism of uranium adsorption onto the adsorbents.

3.3.Batch adsorption experiment and adsorption parameters optimization

The adsorption properties of the adsorbents under study for uranium removal from water were investigated using the batch adsorption method and were caried out in 100 mL glass conical flasks. The process was carried out on a mechanical shaker at 150-rpm shaking speed for three hours at room temperature. Filtration was used to separate the adsorbent using Whatman filter paper. The initial concentration of the solution was 30mg/L. The uranium removal (%) was calculated by the following **Equation 3.1**(Kushwaha and Sudhakar, 2013)

$$Removal\ (\%) = (C_0 - C_e)\ x\ 100/C_0 \qquad \textbf{(3.1)}$$

Where, C_0 is the original concentration and C_e is the final concentration of uranium after adsorption.

Adsorption parameters:

(i) **pH:** pH of the solution plays a significant role in the adsorptive removal of metal ions. Therefore, it is important to optimize the pH condition for adsorption. For this study the pH was varied from 2-10 keeping other parameters such as initial concentration of adsorbate, adsorbent dose, temperature, equilibration time and total volume of solution.

(ii) **Dose:** An essential factor in an adsorption investigation is dosage optimisation. The number of active sites and the mass transfer efficiency are both directly

affected by the dosage of the adsorbent (Zhao et al., 2023). In the context of the economic analysis of adsorption, dose optimisation is equally crucial.

(iii) **Contact time:** Contact time serves as an important component of adsorption optimisation and understand the kinetics of the adsorption process. For this study the contact time was varied keeping other parameters such as initial concentration of adsorbate, adsorbent dose, temperature, and total volume of solution constant.

(iv) **Concentration:** In the current study, the impact of initial concentration on the adsorption by various adsorbents was examined with varying concentrations of metal ion adsorbate under study under optimised conditions of pH, adsorbent dose, and equilibration time.

(v) **Temperature study:** Under ideal circumstances, the effect of temperature on the degree of solute adsorption was systematically examined at various temperatures to understand the thermodynamics of the adsorption process.

The removal capacity post-adsorption was calculated using the **Equation 3.2.**

$$q_e\ (mg/g) = [(C_i - C_e)\ *V]/W \qquad \textbf{(3.2)}$$

where, q_e represents the uranium uptake capacity, C_i and C_e represent the concentration of uranium (mg/l) initial and equilibrium concentration respectively. V stands for the volume of aqueous solution in liter and W is the amount of adsorbent used in gram.

3.4. Isotherms and Kinetics analysis for adsorption study

The adsorption mechanism and maximum adsorption capacity of adsorbate on adsorbents under study were investigated by fitting the sorption data in the respective isotherm and kinetic models. The isotherm models used were Langmuir and Freundlich and the kinetic models explored were pseudo-first order and pseudo-second order. **Table 3.1 and Table 3.2** summarize the assumptions and equations involved in the kinetic and isotherm models studied.

Table 3.1 Models of isotherms and their applicability.

Sr No.	Isotherm model name	Descriptions	Plot	References
1	Langmuir	Langmuir's model assumes that the surface of the adsorbent is homogeneous with identical adsorption sites with	$1/C_e$ vs $1/q_e$	(Langmuir, 1916)

		uniform energies of adsorption and no transmigration of adsorbate. This describes quantitatively the formation of a monolayer adsorbate. Qm indicates maximum adsorption capacity		
2	Freundlich	The constant K_f is an approximate indicator of adsorption capacity, assumes heterogeneous multilayer adsorption while 1/n is a function of the strength of adsorption process which varies with the heterogeneity of the material. The value of 1/n predicts whether the adsorption process is favourable (0.1 < 1/n < 0.5) or unfavourable (1/n > 2).	Log C_e vs Log q_e	(Freundlich, 1906)

The above-mentioned isotherms have been applied to explain the equilibrium adsorption characteristics. **Equation (3.3)** represents Langmuir's isotherm, and its linear form is represented by **Equation (3.4)**

$$qe = \frac{qmax\ KL\ Ce}{1+KL\ Ce} \qquad \textbf{(3.3)}$$

$$C_e/q_e = 1/K_L q_{max} \times C_e + 1/q_{max} \qquad \textbf{(3.4)}$$

where, q_{max} represents the maximum adsorption capacity (mg/g) and K_L (L/mg) is Langmuir's isotherm constant which shows the binding affinity between uranium and adsorbents.

The separation factor (R_L) is calculated using **Equation (3.5).**

$$R_L = \frac{1}{1+Ci*KL} \qquad \textbf{(3.5)}$$

where, R_L is the dimensionless Langmuir constant which indicates the adsorption feasibility either favorable ($0 < R_L > 1$), unfavorable ($R_L > 1$), linear ($R_L = 1$) or irreversible ($R_L = 0$).

Equation (3.6) represents the Freundlich's isotherm and **Equation (3.7)** its linear form

$$qe = Kf\ Ce^{1/n} \qquad \textbf{(3.6)}$$

$$logqe = logKf + \frac{1}{n} log\ Ce \qquad (3.7)$$

where, K_f is Freundlich's constant

Present study focuses on the pseudo-1st-order and pseudo-2nd-order kinetics models.

Table 3.2. Kinetic models with their applications.

Sr No.	Kinetics model name	Descriptions	Plotting	References
1	Pseudo-1st-order	The kinetic model generally does not fit throughout the whole adsorption cycle, it is generally at the initial stage. The amount of uptake capacities generally increases with an increase in time and concentration.	t vs ln(q_e-q_t)	(Lagergren, 1898)
2	Pseudo- 2nd - order	The kinetic model generally supports the chemisorption of adsorbate during the adsorption process.	t vs t/q_t	(Ho, 2006)

The pseudo 1st order is represented in **Equation (3.8).**

$$ln\ (q_e - q_t) = lnq_e - K_1\ t \qquad (3.8)$$

Where, q_t represents the adsorption capacity (mg/g) at time t while K_1 (min^{-1}) is the equilibrium rate constant.

Pseudo 2nd order is represented in **Equation (3.9)**:

$$\frac{t}{qe} = \frac{1}{K_2\ q_e^2} + \frac{1}{qe} \qquad (3.9)$$

where K_2 (g $mg^{-1}min^{-1}$) is the equilibrium rate constant. The values of linear coefficient regression (R_2) are used to predict the most suited isotherm and kinetic model for the adsorption process.

The thermodynamic parameters of the adsorption process was determined for the experimental data using **Equation 3.10**:

$$\Delta G^0 = \Delta H^0 - T\Delta S^0 \qquad (3.10)$$

Where, ΔG^{o} =Gibbs free energy ($kJmol^{-1}$), ΔH^{o} =enthalpy ($KJ\ mol^{-1}$), T=absolute temperature (K), and ΔS^{o} = entropy ($JK^{-1}\ mol^{-1}$).

3.5. Desorption study

Desorption studies are important in determining whether recovery of pollutants after adsorption is feasible and whether the regeneration of the adsorbent for further usage is possible or not. Eluent, or desorbent solution, is used in the desorption process to treat the exhausted adsorbent. Adsorbate releases from adsorbent when the bond between both of them breaks. The adsorption procedure continues on this treated adsorbent. Anionic and cationic contaminants are typically desorbed using alkaline solutions, preferably NaOH, and acidic solutions, usually HCl, this is because of electrostatic attraction, which signifies that the pH factor mostly influences the desorption mechanism (Patel, 2021). The adsorption-desorption investigation was conducted under optimal conditions. The percentage of metal ion desorbed from the adsorbents loaded with adsorbate was calculated by using **Equation 3.11.**

$$\%\ desorption\ = \frac{q_{des}}{q_{ads}} \times 100 \qquad \textit{(3.11)}$$

Where, q_{des} is desorbed uranium content (mg/l) and q_{ads} is absorbed uranium content.

The present chapter is divided into two sections. **Section A** of the present chapter comprises of chitosan DTPA (Diethylenetriamine pentaacetic acid) synthesis, characterization and its application in removal of uranium while **Section B** describes synthesis of watermelon rind biochar, characterization and its application in removal of uranium.

Chapter 3A

Synthesis of Chitosan-DTPA for Removal of Uranium from Aqueous Solution

3A.1.Materials and Methods

3A.1.1.Materials and chemicals: Chitosan (from crab shells) (87.6 % deacetylated) was purchased from Sigma-Aldrich. Diethylenetriaminepentaacetic acid (DTPA) (98% and molecular weight 393.35) was purchased from Spectrochem. Uranyl Nitrate Hexahydrate puriss AR $UO_2(NO_3)_2.6H_2O$ which was purchased from Spectrochem PVT.LTD. All chemicals were procured and used without any further purification.

3A.1.2.Preparation of Chitosan DTPA: In the first step 1mLglacial acetic acid (GAA) was taken in a conical flask and 1% of chitosan was added while stirring. In the second step, 3.93g of diethylenetriaminepentaacetic acid (DTPA) was dissolved in 100 mL of 0.5N NaOH solution to make 0.1N DTPA solution. Further the DTPA solution was then slowly added to the chitosan solution (v/v) with continuous stirring for 4 hours at room temperature. The solution was then filtered using Whatman filter paper. The obtained residue was washed with distilled water till neutral pH and dried in oven at 80^0C. The dried product was crushed into fine powder using mortar and pestle and was used as adsorbent further for the uptake study of Uranium. **Figure. 3A.1.** show a schematic representation of the chitosan-DTPA synthesis.

3A.1.3.Preparation of uranium solution: Stock solution was prepared by dissolving 2.11g Uranyl Nitrate Hexahydrate puris AR [$UO_2(NO_3)_2.6H_2O$] in 1L conductivity water to obtain 1000mg/L of stock solution. Working standards were prepared by diluting different volumes of the stock solution to obtain the desired concentration.

3A.1.4.Determination of uranium uptake capacity: The entire study was carried through a batch process as described in section 3.3. Uranium concentration was estimated in the filtrate obtained after filtration, using Agilent Technologies model no. Cary 60 UV-Vis spectrophotometer at wavelength of 651nm by complexation of Arsenazo III reagent with uranium solution (Khan et al., 2006). Uranium uptake per gram of CH-DTPA was calculated using **Equation 3.2.**

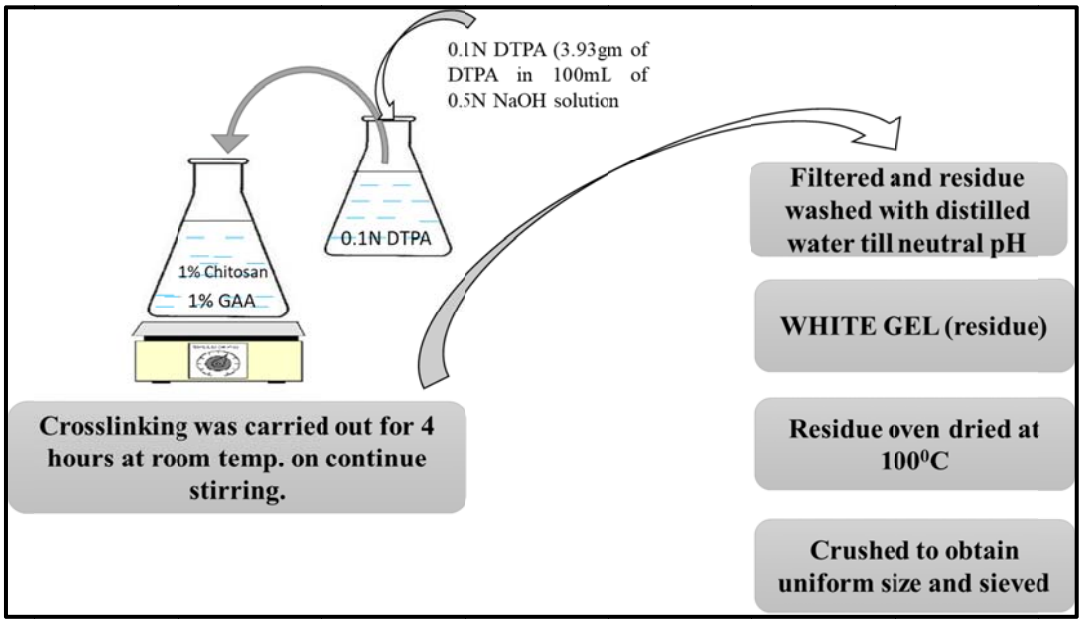

Fig. 3A.1. Synthesis of chitosan-DTPA

3A.2.Results and Discussion

3A.2.1.Effect of pH on the uptake of uranium: The pH effects on the uptake of uranium (30mg/L) from aqueous solution by Chitosan-DTPA was studied in the pH range 2 to 10 at room temperature by equilibrating for 1 h**.** The uptake of uranium was found to be maximum (>98%) in the pH range 4-7 **(Figure 3A.2a**). There was an uptake of 98.55% uranium at neutral pH and so, pH 7 was selected as the optimal pH for subsequent adsorption studies.

3A.2.2.Effect of adsorbent dosage on the uptake of uranium: The effect of variation of adsorbent dosage on the removal of uranium pertaining to this study is shown in (**Figure 3A.2(b))** from which it can be concluded that for a fixed initial uranium concentration, increasing the adsorbent dose provided greater surface area and availability of more active sites (Sharma et al., 2020), thus leading to the enhancement of metal ion uptake. Adsorption increased from 54.23% (5mg dose) to >99% (50mg dose) with the increase in adsorbent dose. An optimum dose of 35mg was selected for further studies.

3A.2.3.Effect of contact time on the uptake of uranium: Figure 3A.2(c) depicts the effect of contact time. Experiments were conducted by equilibrating 25 mL of 30 mg/L uranium solution at pH 7 with 0.035 g of CH-DTPA for various time periods (10 to 360 minutes), to optimize the impact of contact time. Fast and maximum uranium adsorption up to 80% was observed in the initial 30 min and finally equilibrium was attained in 60 min. This fast-

kinetics behavior indicated that the adsorption process depends upon the available binding sites on CH-DTPA for the uptake of uranium. After 60 minutes, the adsorption surface became saturated with the adsorbate, and finally, dynamic equilibrium was achieved.

3A.2.4.Effect of concentration on the uptake of uranium: The effect of concentration on the uptake of uranium was depicted in (**Figure 3A.2(d)**) where with increase in concentration there was a decline in the uptake of uranium from 99.9% to 81.83% for 20mg/L to 150mg/L respectively due to the saturation of the adsorption sites.

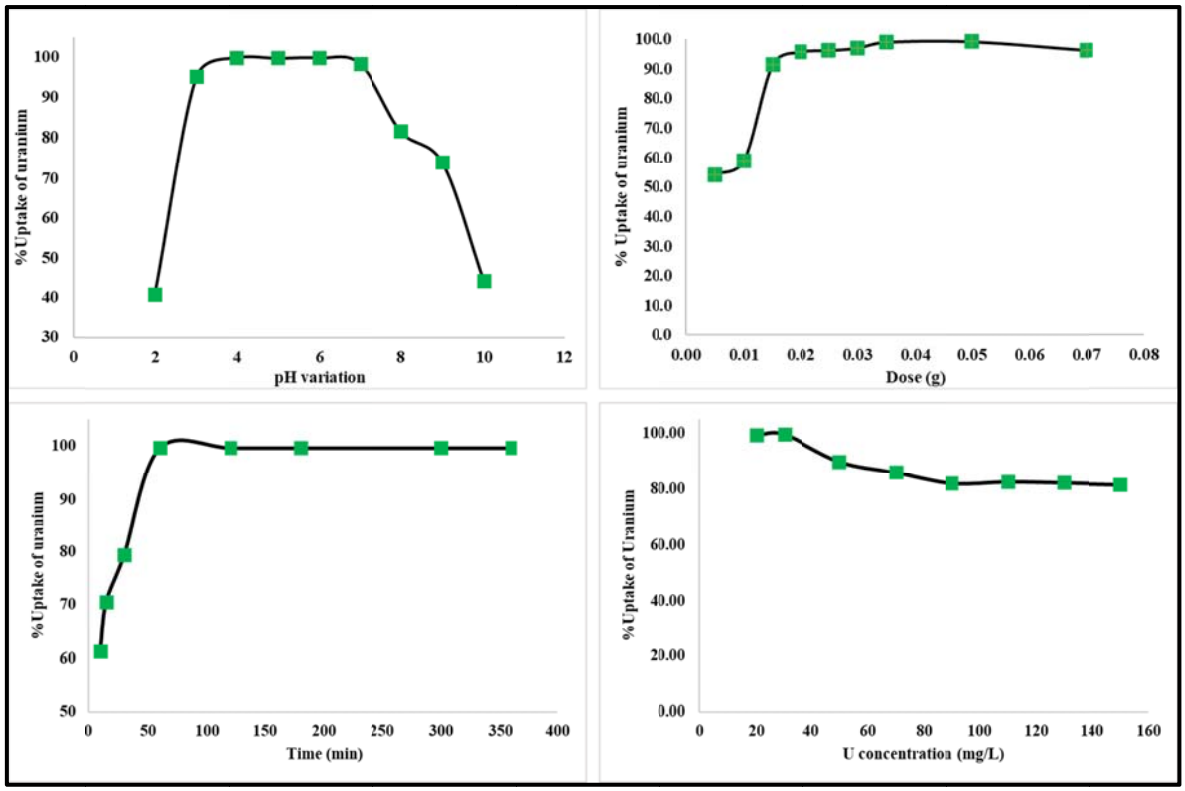

Fig. 3A.2 (a) Effect of pH **(b)**Effect of adsorbent dosage **(c)** Effect of contact time and **(d)** Effect of Concentration on the adsorption of Uranium by CH-DTPA

3A.2.5.Kinetic studies: In the present study, the pseudo 1st and 2nd order rate equations **(Equations 3.8 and 3.9 respectively)** were used to further evaluate the kinetic parameters of uranium on CH-DTPA. The fitting of the two kinetic models to the uranium adsorption data are shown in (**Figure 3A.3(a) and (b)**) and the results of respective kinetic parameters are shown in **Table 3A.1**

The pseudo 2nd order kinetics proved to be a better fit model with respect to kinetics of uranium adsorption on CH-DTPA as it showed a higher value of linear regression coefficient (R^2 >0.99) when compared with the pseudo1st order model (R^2 <0.60). Further, the q_e value

was very close to the experimental q_e value suggesting chemisorption to be limiting step in adsorption of uranium involving valent forces through the exchange of electrons between adsorbent and adsorbate, complexation, coordination or chelation(Ayub et al., 2020; Kushwaha and Sudhakar, 2013).

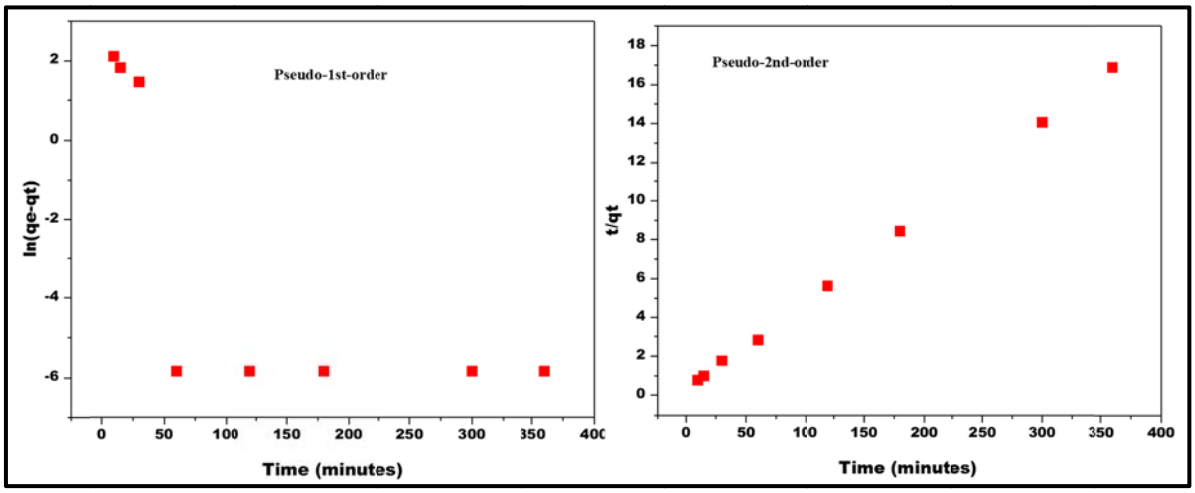

Fig. 3A.3 (a) and **(b)** Pseudo 1st order and Pseudo 2nd order kinetics plots for the sorption of uranium onto CH-DTPA (operating parameters: pH 7, conc. 30mg/L, dose 35mg, volume 0.025L, room temp.).

Table 3A.1 Kinetic parameters for the removal of uranium by CH-DTPA.

Pseudo 1st order			**Pseudo 2nd order**			
q_e (mg/g)	**K_1**	**R^2**	**q_e (exp)**	**q_e (mg/g)**	**K_2**	**R^2**
1.856179	2.14×10^{-4}	0.51	21.36	21.75	9.120×10^{-3}	0.999

3A.2.6.Adsorption Isotherms: In the present study the data was fitted to Langmuir and Freundlich isotherm models as shown in (**Figure 3A.4 (a) and (b)) respectively**. The pertaining values of the same are shown in **Table 3A.2**. According to the data of Langmuir and Freundlich, Langmuir isotherm was a better fit as compared to Freundlich isotherm. The results imply that uranium was adsorbed by a monolayer adsorption mechanism on a homogenous surface. The comparison of the synthesized adsorbent with the various adsorbents reported in literature with respect to the adsorption capacities have been tabulated in **Table 3A.3**

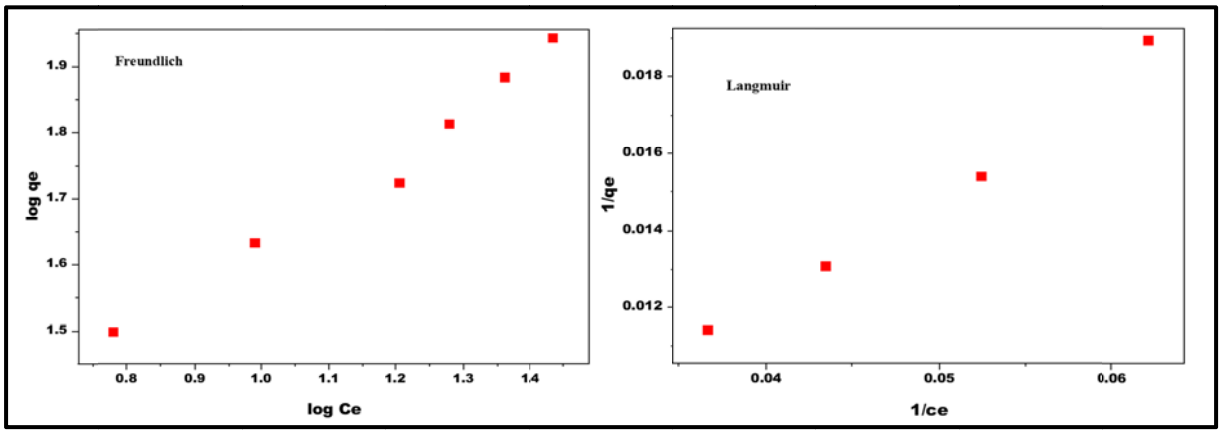

Fig. 3A.4. Adsorption Isotherms for uranium on CH-DTPA (operating parameters; 20-150mg/L, pH 7, time 60min, dose 35mg, room temp, volume 0.025L)

Table 3A.2. Isotherm parameters for adsorption of uranium on CH-DTPA

Freundlich isotherm			**Langmuir isotherm**			
1/n	**Kf**	**R^2**	**q_{max} (mg/g)**	**K_L (dm^3/mg)**	**R_L**	**R^2**
0.67	9.26	0.97	2500.0	0.0014	0.961	0.990

Table 3A.3. Comparison with other reported chitosan derivatives as adsorbents.

Sr. No.	**Adsorbents**	**Qmax (mg/g)**	**pH**	**References**
1	Chitosan with epichlorohydrin (CCTS)	72.46	3	(Wang et al., 2009)
2	The chitosan-coated natural attapulgite beads (CNAB)	264.55	5.5	(Pang et al., 2010)
3	Chitosan-tripolyphosphate (CTPP)	236.9	5	(Sureshkumar et al., 2010)
4	An interpenetration network (IPN) ion-imprinting hydrogel (IIH)-cross-linked chitosan (IIH)	156.0	5	(Liu et al., 2010)
5	Ethylenediamine-modified magnetic chitosan (EMMC)	82.83	3	(Wang et al., 2011)
6	Pure chitosan gels (PCS)	483.05	5	(Liu et al., 2011)
7	Glutaraldehyde-chitosan gels (GLACG)	147.05	4	
8	Epichlorohydrin-chitosan gels (ECCS)	334.83	4	
9	Ethylene glycol diglycidyl ether-chitosan gels (EGDECS)	54.02	5	
10	ion-imprinted magnetic chitosan resins (IMCR)	187.26	5	(Zhou et al., 2012)
11	A novel adsorbent poly(methacrylic acid)-grafted chitosan/bentonite (CTS-g-PMAA/Bent) composite	117.2	5.5	(Anirudhan and Rijith, 2012)
12	The Saccharomyces cerevisiae-crosslinked chitosan-magnetic nanoparticle (SC-CTS-ECH-MNP)	72.4	4	(Saifuddin and Dinara, 2012)

13	Modified magnetic chitosan resin containing diethylenetriamine functional groups (DETA-MCS)	65.16	3.5	(Xu et al., 2013)
14	Triphosphate-crosslinked magnetic chitosan resins (TPP-MCR)	169.4	4	(Zhou et al., 2014)
15	Cysteine-Functionalized Chitosan–Magnetic Nano-Based Particles (Cysteine/chitosan magnetic nanoparticles)	97.5	3.61 - 5	(Galhoum et al., 2015)
16	Phosphorylated chitosan (P-chitosan)	54.4	5	(Morsy, 2015)
17	Magnetic hydrothermal cross-linked chitosan (HCC–Fe_3O_4)	263.1	7	(Yu et al., 2016)
18	Magnetic carboxymethyl chitosan nanoparticles functionalized with ethylenediamine (EDA-MCCS)	175.6	4.5	(Zhou et al., 2016)
19	Amidoxime functional chitosan beads (MAO-chitosan)	117.65	6	(Zhuang et al., 2018)
20	Chitosan	68	5	(Mishima et al., 2018)
21	Magnetic chitosan/graphene oxide composites (MCGO)	178.6	5	(Huang et al., 2018)
22	Polyvinylpyrrolidone/Chitosan blended nanofibers (PVP/chitosan fibers)	167	6	(Christou et al., 2019)
23	Electrospun chitosan/baker's yeast nanofibre (CS NFs)	59.87	<6	(Rostamian et al., 2019)
24	Amidoxime functionalized adsorbent, poly(amidoxime)-grafted-chitosan/bentonite composite (P(AO)-g-CTS/BT)	49.09	8	(Anirudhan et al., 2019)
25	2-phosphonobutane1,2,4-tricarboxylic acid-decorated chitosan-coated magnetic silica (CoFe2O4@SiO2@CS-PBTCA)	105.26	4	(Huang et al., 2020)
26	Chitosan grafted titanium dioxide (CS/TiO_2)	163.2	5	(Wang et al., 2020)
27	Chitosan-based aerogel (CS-PTA-DMAs)	160	6	(Yang et al., 2021)
28	Chitosan grafted phenylenediamine polysulfone (PSu) – (PSu/C-g-PDA)	44	3	(Orabi et al., 2021)
29	Chitosan grafted phenylenediamine cellulose acetate (CA)- (CA/C-g-PDA)	39		
30	Chitosan/Chlorella pyrenoidosa composite adsorbent bearing phosphate ligand (CSP/CP)	1393.33	5	(Liu et al., 2022)
31	Chitosan-DTPA (CH-DTPA)	2500	7	Present study

The adsorption capacity is at a neutral pH compared with the previous study. It was found that the adsorption capacity was highest reported till date.

3A.2.7.Thermodynamic parameters: The thermodynamic parameters such as change in free energy (ΔG°), enthalpy (ΔH°), and entropy (ΔS°) as calculated from **Equation 3.10** were obtained for the adsorption of uranium on CH-DTPA and have been given in **Table 3A.4.** The negative value of ΔH^0 indicated the feasibility and spontaneous nature of adsorption process of uranium on CH-DTPA and that the adsorption process was exothermic (Noli et al., 2019). Also, a decrease in randomness at the solid/solution interface during the uranium adsorption process on CH-DTPA was indicated by the negative entropy value (Ebisike et al., 2023).

Table 3A.4. Thermodynamic data of uranium on CH-DTPA

Temp. (K)	K_L	ΔG^0 KJmol^{-1}	ΔH^0 KJ mol^{-1}	ΔS^0 JK $^{-1}$ mol^{-1}	R^2
293	213.57	-13.067	-155.774	-485.883	0.699
298	213.57	-13.290			
303	9.63	-5.706			
313	5.80	-4.574			

3A.2.8.Reusability and recyclability study of CH-DTPA: The desorption of uranium ions adsorbed onto CH-DTPA was investigated with 0.5 M and 1M NaOH, HCl and Na_2CO_3 solutions. It was observed that maximum desorption was achieved with Na_2CO_3 solution 0.1M Na_2CO_3 solution was utilized for desorption of CH DTPA which was equilibrated with 30mg/L of uranium in order to investigate the reusability of the adsorbent. The adsorbent was dried and utilized again for the adsorption process after desorption. Up to four cycles of the adsorption-desorption experiments were carried out **(Figure. 3A.5).** The desorption % was calculated using **Equation 3.11.** In the fourth cycle, the adsorption efficiency decreased to 75%. Uranium could thus be desorbed within 60 minutes using CH-DTPA and reused up to 3 cycles with greater than 90% efficiency.

3A.2.9.Effect of Electrolytes: The removal efficiency of the adsorbents was examined in the presence of electrolytes, by investigating the adsorption of uranium in the presence of electrolytes such as $NaNO_3$, $NaHCO_3$, Na_2SO_4, NaCl, and Na_2CO_3 under optimized conditions (**Figure 3A.6.)**. The investigation revealed that sodium bicarbonate and sodium

carbonate inhibit uranium's ability to adhere to CH-DTPA due to formation of soluble $(UO_2)_2CO_3(OH)_3^-$.

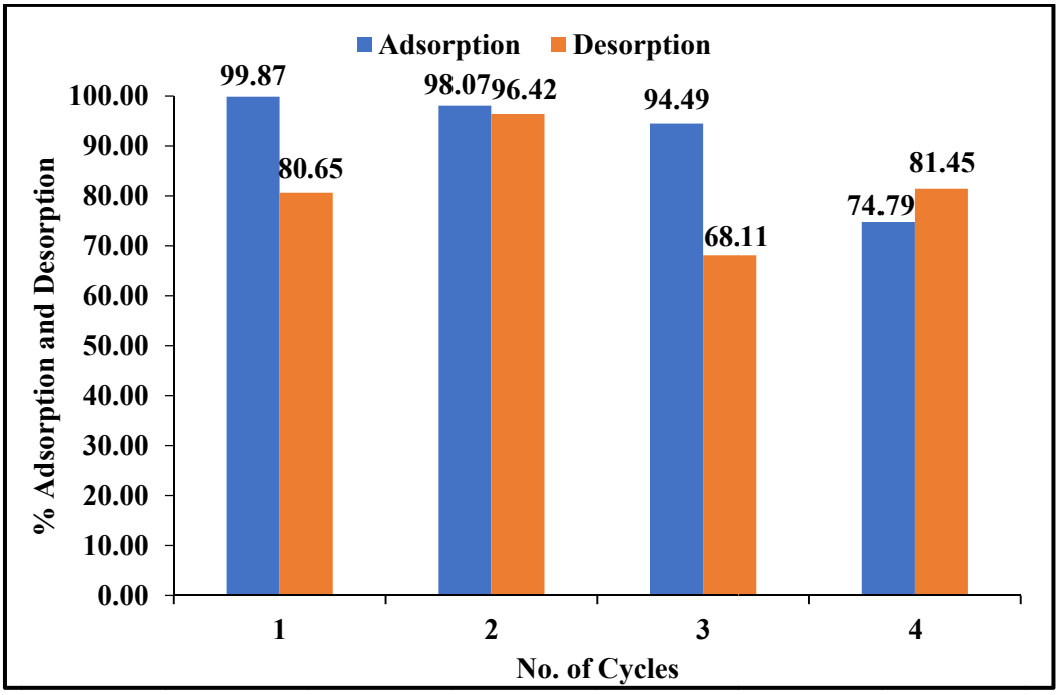

Fig. 3A.5. Uptake of uranium after consecutive 1st 2nd, 3rd, and 4th cycles using 1M Na_2CO_3 as regenerant (Initial dose: 35 mg, initial U concentration: 30 mg/L, time: 60min. volume 0.025L)

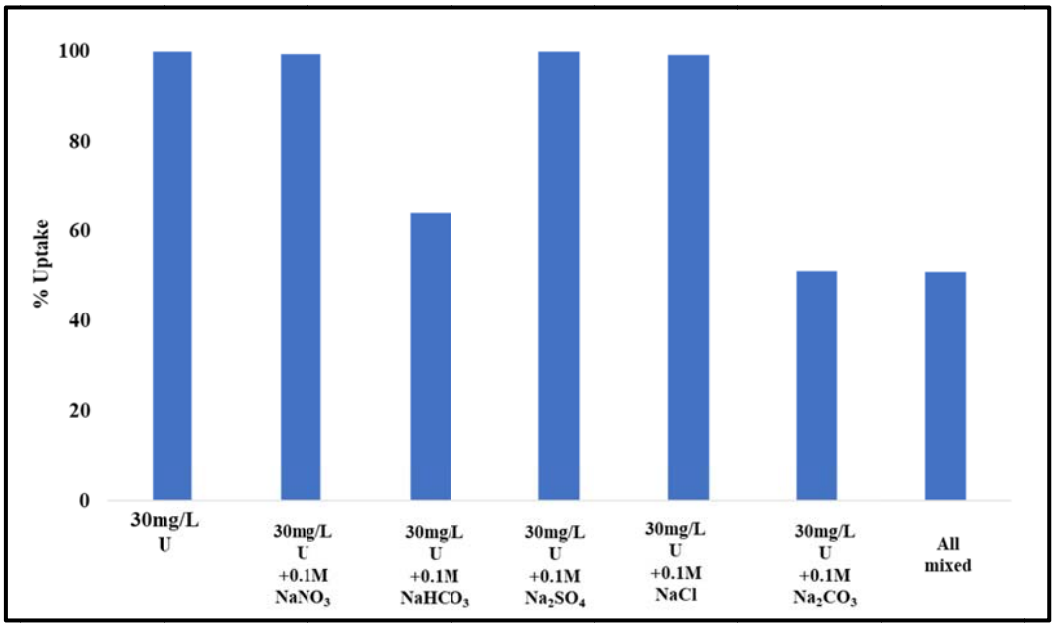

Fig.3A.6. Effect of electrolytes on the adsorption capacity of uranium

3A.2.10.Application to real water sample (groundwater): Adsorption of uranium using CH-DTPA from groundwater water sample collected from Department of Environment Studies was studied after spiking the samples with different concentrations of uranium (20, 30, and 50 mg/L), under optimised conditions (pH: 7.37, dose:35mg, time: 3h, volume:0.025L). Physico-chemical parameters of the collected groundwater sample are listed in **Table 3A.5**.

Table 3A.5. Physicochemical properties of groundwater sample.

S.N.	Parameters	Conc.	S.N.	Parameters	Conc.
1	pH	7.37	10	Cl^- (mg/L)	294.91
2	TDS (mg/L)	837	11	TA (mg/L)	780
3	EC(µs/cm)	1675	12	HCO_3^- (mg/L)	780
4	DO	2.2	13	TH (mg/L)	262.24
5	Temp.(ºC)	29.2	14	CaH (mg/L)	55.47
6	F^-(mg/L)	3.11	15	MgH (mg/L)	206.76
7	NO_3^- (mg/L)	1.65	16	Na^+ (mg/L)	45
8	SO_4^{2-}(mg/L)	122.1	17	K^+ (mg/L)	92
9	PO_4^{3-}(mg/L)	0.71	18	U (mg/L)	00

Groundwater spiked with a 20mg/L uranium solution exhibited 25 percent removal at pH 7 due to possible interference by bicarbonate and formation of soluble uranium carbonate complex. The interference can be overcome by performing the adsorption process at pH 4 to 5.

3A.3.Characterization of CH-DTPA and after adsorption of uranium (CH-DTPAU):

CH-DTPA before and after uranium adsorption was characterized to understand the adsorption mechanism and characteristics of the material.

3A.3.1.FT-IR analysis: The FTIR spectra of the CH-DTPA before and after uranium adsorption are can be seen in (**Figure. 3A.7)**. The FTIR spectrum of CH-DTPA showed a characteristic N-H stretching vibration at 3439.85 cm^{-1} and C-H stretching at 2926.66 cm^{-1}. Bands at 1072.87 cm^{-1} ,1219.41 cm^{-1}, and 1072.87 cm-1 were attributed to C=O, C-O, C-N

stretching respectively (Bhatt et al., 2015). The band observed at ~1645.0 cm^{-1} due to N-H bending vibration of amide indicated the formation of amide bond in CH-DTPA. The 772.45 cm^{-1} peak in CH-DTPA attributed to O-C-O bending mode as well as the 1219 cm^{-1} band attributed to C-O stretching diminished after adsorption of uranium, indicating the binding of uranium on CH-DTPA.

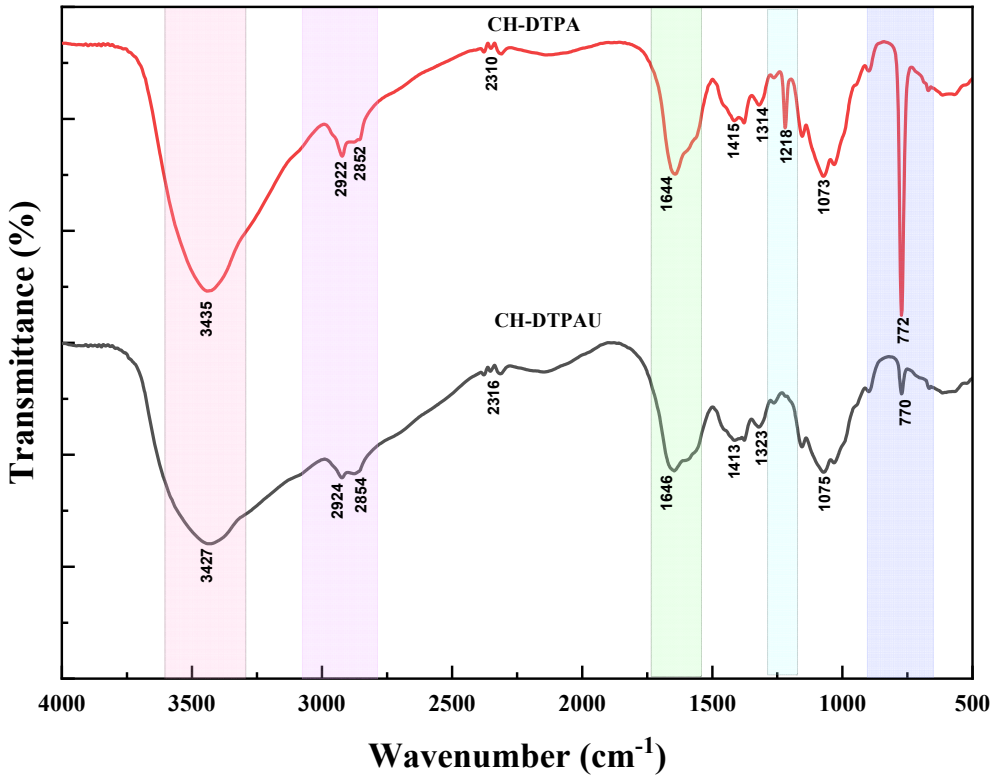

Fig. 3A.7. FTIR spectra of CH-DTPA and CH-DTPAU

3A.3.2.SEM analysis: The surface morphology of chitosan -DTPA was observed by SEM before and after uranium adsorption (**Figure 3A.8. (a) & (b)**). The surface of chitosan-DTPA had a bright white color after adsorption of uranium supporting the successful adsorption of uranium by CH-DPTA with no significant change in morphology.

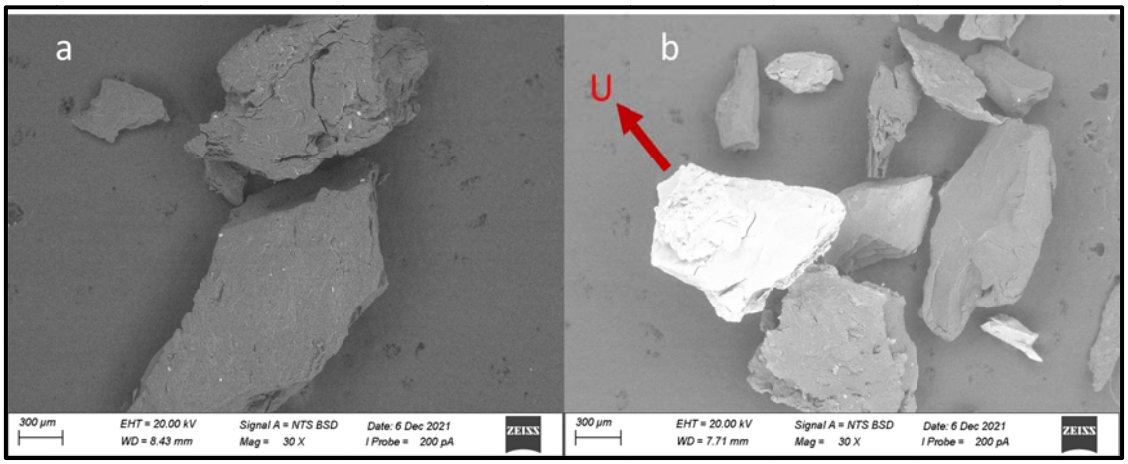

Fig. 3A.8. SEM images of (a) CH-DTPA and (b) CH-DTPAU.

3A.3.3.EDX analysis: The elemental composition of the CH-DTPA both before and after uranium uptake was evaluated using the EDX technique **(Figure. 3A.9 a&b)**, The uptake of uranium on the surface as seen in (**Figure 3A.9(b))** supported the adsorption of uranium on CH-DTPA with no signifiicant change in composition.

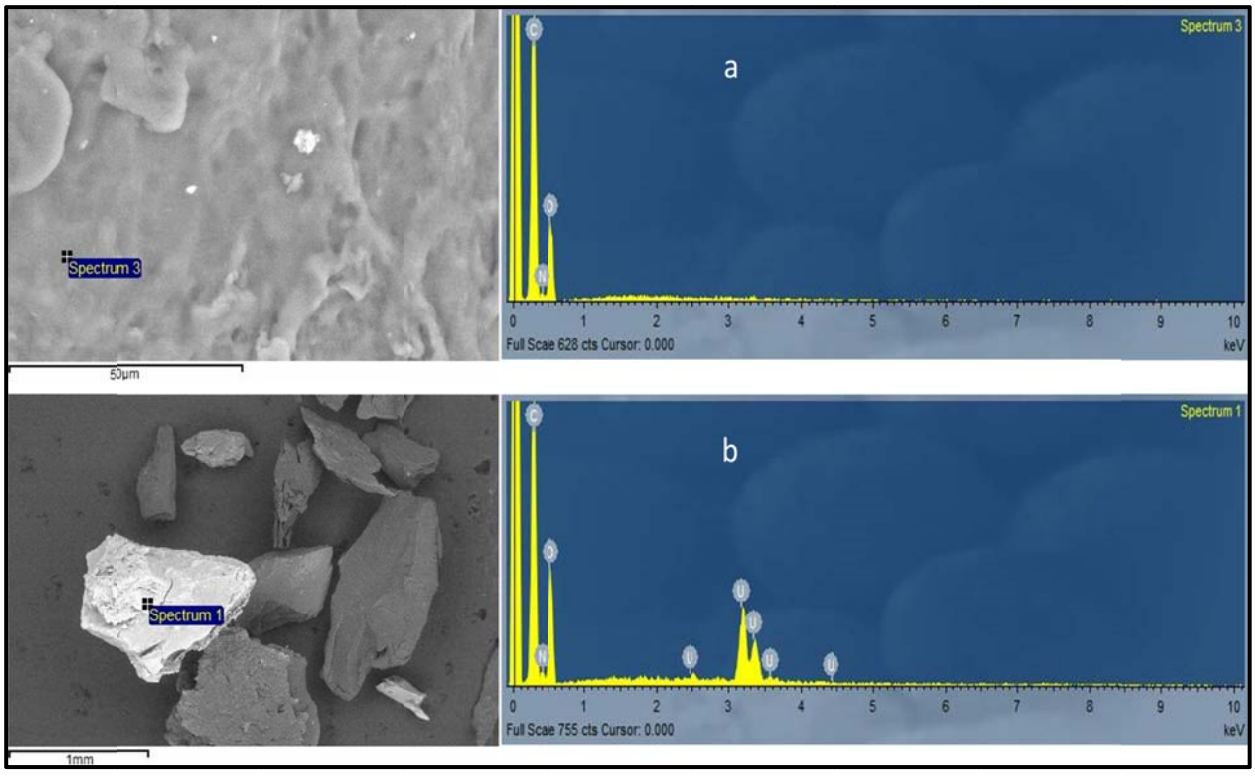

Fig.3A.9. EDS data of (a) CH-DTPA and (b) CH-DTPAU.

3A.3.4.Thermal analysis(TGA): Fig. 3A.10(a) & (b) shows the thermogram of CH-DTPA and CH-DTPAU. The first major weight loss was seen from 50-250^{0}C in CH-DTPA

corresponding to the evaporation of water and moisture, which was around 12.5% of total weight of CH-DTPA. The second stage started at 250ºC and reached a maximum at 380ºC with a weight loss of 61.1% and was attributed to deacetylation of CH-DTPA, vaporization, and elimination of volatile products (Neto et al., 2005). The final weight loss after 400ºC due to almost complete decomposition and volatilization was observed to be 17.1 %. As seen in (**Figure 3A.10)** weight loss of 12.5% was observed for CH-DTPAU in the region of 50-250^{0}C which corresponded to the loss of water bound in the matrix. The second weight loss seen was in the region of 250-350^{0}C which accounted for 39.6% of weight loss and the final weight loss was of 8.2% in the region of 350-500^{0}C.

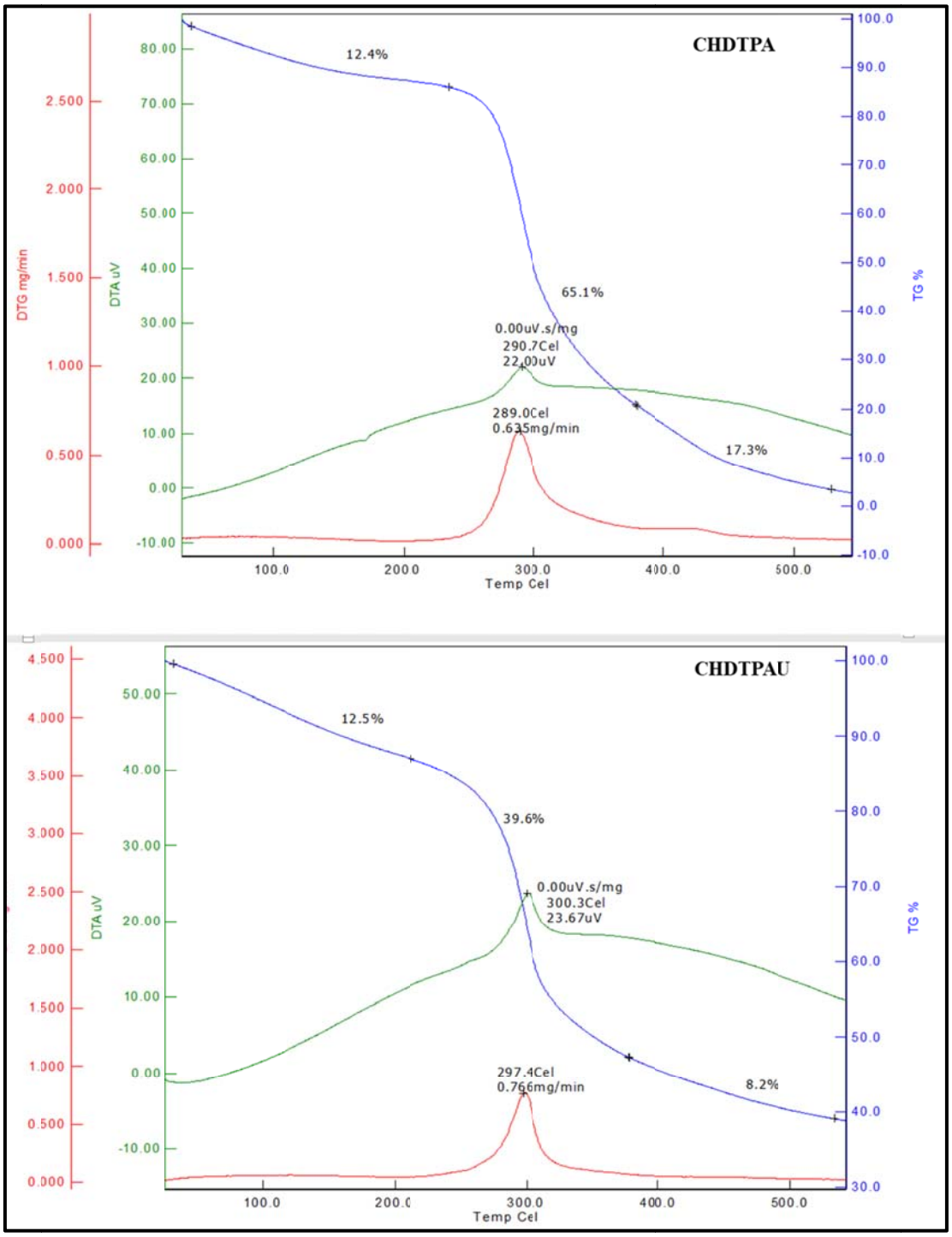

Fig.3A.10. Thermogravimetric (TGA) curves for CH-DTPA and CH-DTPAU.

3A.3.5.X-ray diffraction analysis (XRD): Figure 3A. 11 (a) & (b) shows the XRD pattern of Chitosan-DTPA before and after adsorption of uranium. A notable broad diffraction peak was seen at (2θ = ≈28.02^0), indicative of the semi-crystalline nature of CH-DTPA. After uranium adsorption, the XRD pattern of CH-DTPA **(Figure 3A.11(b))** reveals a few more crystalline peaks corresponding to uranium adsorption. In CH-DTPAU diffraction pattern, the

peak at 21.4º was attributed to (001) diffraction plane of U_3O_8 (which was seen as a part of the broad peak observed for chitosan at 20.48º) and the diffraction peak at 44.3º was attributed to (002) plane while the shoulder observed at 28.02º was assigned to the (111) plane of the cubic UO_2 phase (JCPDF 41-1422) (Lin et al., 2014).

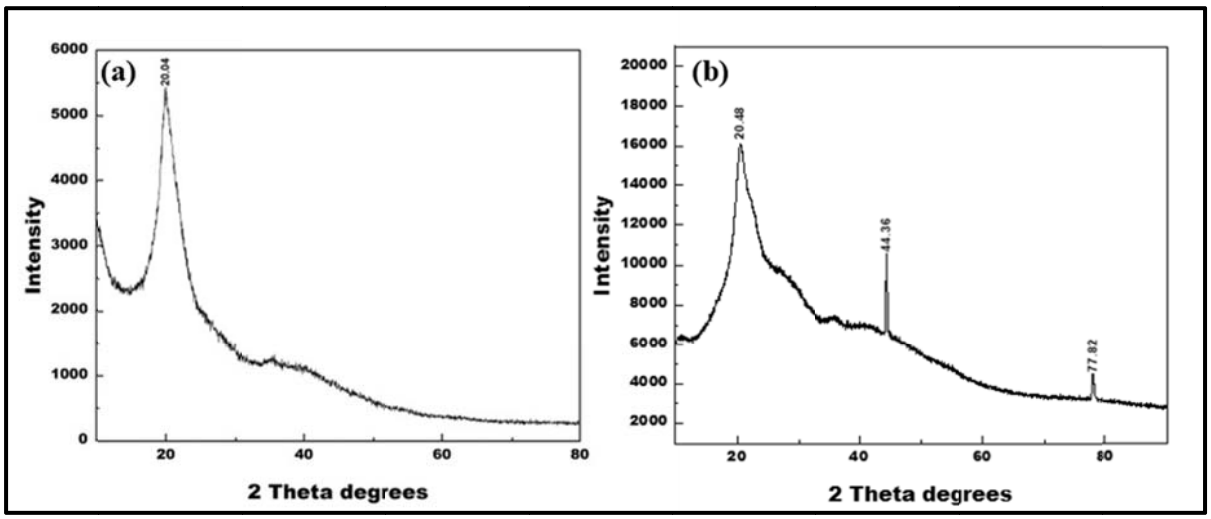

Fig. 3A.11. XRD plots of **(a)** CH-DTPA and **(b)** CH-DTPAU.

3A.3.6.XPS analysis: The chemical composition and states of the individual components were examined using XPS. The survey spectrums of CH-DTPA and CH-DTPAU are displayed, respectively, in **Figure 3A.12(a)&(b).** After uranium adsorption on CH-DTPA, a distinct uranium peak can be confirmed in the spectra **(Figure 3A.12b).** XPS analysis was further used to study the adsorption mechanism of uranium on CH-DTPA. As shown in **Figure 3A.12 (a)&(b)** respectively, peaks for C1s, N1s, and O1s were identified in the spectra of CH-DTPA before and after adsorption of uranium. After uranium adsorption, the peaks of U4f 7/2 and U4f5/2 appeared **(Figure. 3A.12 b**), indicating that uranium was loaded onto CH-DTPA. For O1s, N1s, and C1s, the atomic percentages of CH-DTPA were 45.37%, 6.94%, and 47.70%, in that order. On the other hand, in the case of CH-DTPAU the atomic percent of O, N, U, U, and C were 48.09%, 6.39%, 0.216%, 2.58%, and 42.72%, respectively. The peak at binding energies 378.6 eV and 389.4 with satellite at 386.9 eV was attributed to U(IV) species while the peaks at binding energies 380.75 and 390.73 eV correspond to U (V) species (Bera et al., 1998; Ilton et al., 2007). The deconvoluted spectra of C1s and O1s (**Figure 3A.12d, e, f, & g)** shows the distribution of the various carbon and oxygen species in DTPA and DTPAU. It could be seen in **Figure 3A.13 a&b**, that the intensity of N1s spectra also changed significantly before and after uranium adsorption on CH-DTPA. The C1s spectrum of CH-DTPA comprised of two peaks at binding energies

287.44 eV and 285.99 eV assigned to C=O and C-C bonds respectively. However, after uranium adsorption on CH-DTPA, a new peak was observed at 283.6 eV attributed to U-C-O bond. Furthermore, the peak of O1s of the C=O/C-O group shifted to lower energy of binding with values from 532.57eV to 531.eV after uranium was adsorbed on to CH-DTPA **(Figure 3A.12 g)** indicating that O atoms in the C=O/C-O group shared electrons with the uranium during complexation to form U=O bonds (Michailidou et al., 2021). The N1s species deconvoluted spectra of CHDTPA and CH-DTPAU are depicted in **Figure 3A.12h&i**. Prior to uranium adsorption, N1s has two distinct peaks 399.98 eV and 399.03eV that correspond to amine groups of DTPA and chitosan. However, after uranium adsorption on CH-DTPA, the binding energy of N1s was shown to have changed from 399.98 to 400.2 eV. This could be because of the uranium-amino group chelation, which altered the electron's surrounding environment and slightly raised the binding energy (Wang et al., 2022)

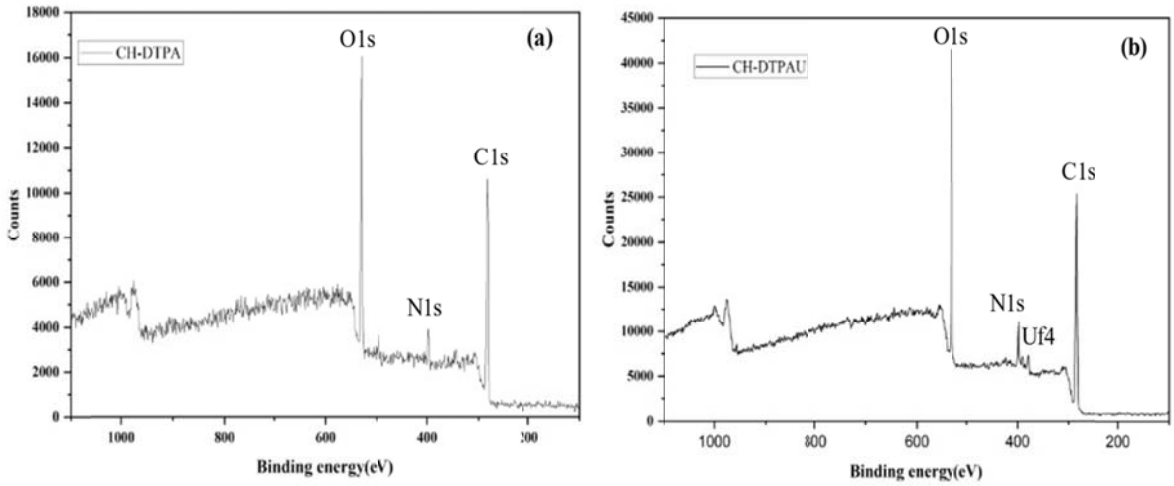

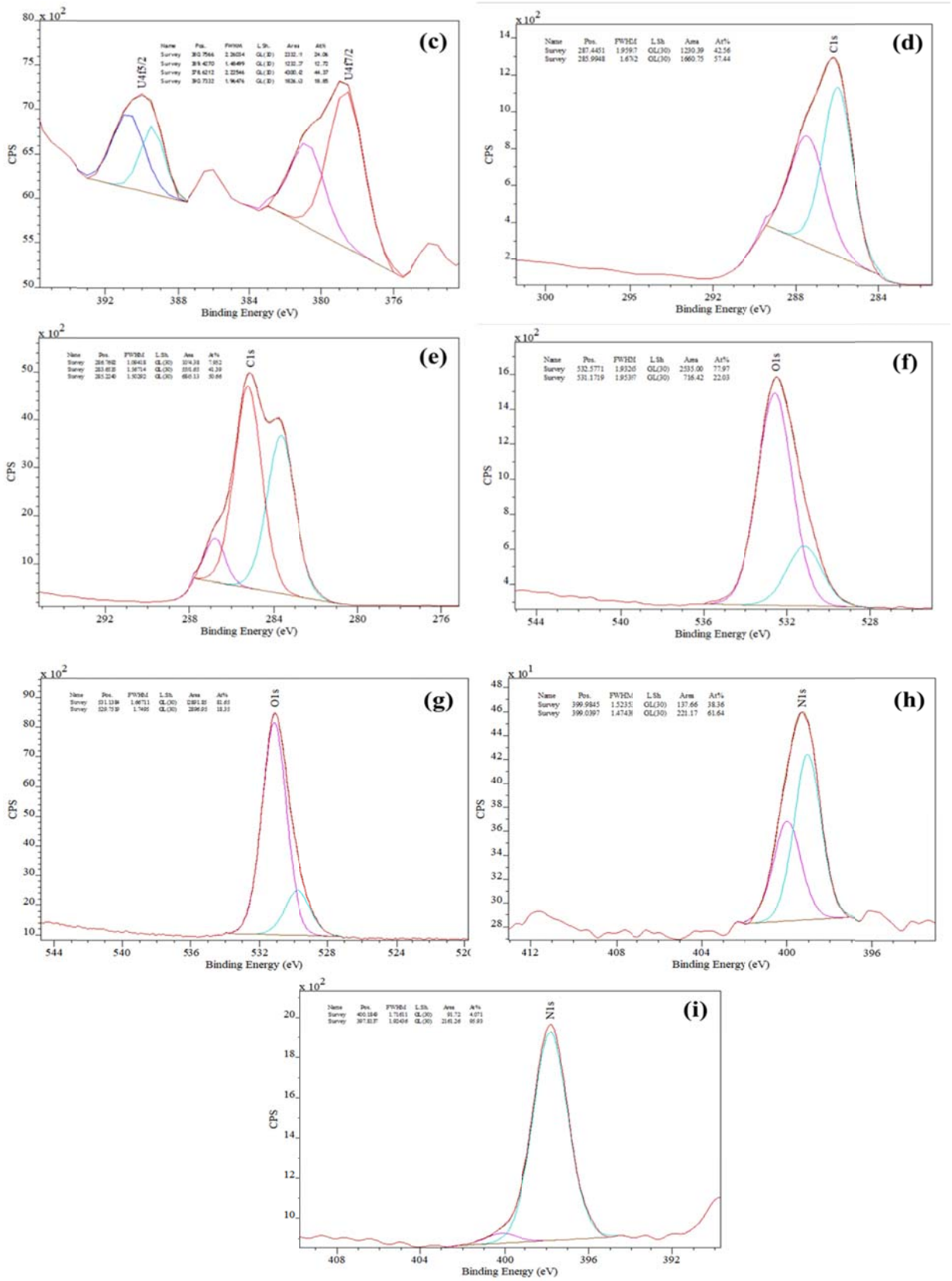

Fig. 3A.12. XPS s **(a)** survey spectra of CH-DTPA **(b)** survey spectra of CH-DTPAU, Deconvoluted spectra of **(c)** U4f in CH-DTPAU; C1s of **(d)** CH-DTPA**, (e)** CH-DTPAU; O1s of **(f)** CH-DTPA , **(g)** CH-DTPAU; N1s of **(h)** CH-DTPA, **(i)** N1s of CH-DTPA

Conclusion

- The chitosan-DTPA adsorbent was fabricated and examined using TGA, FT-IR, XRD, BET, SEM-EDS, and XPS techniques. XPS, revealed the presence of carboxyl and amino groups confirming the formation of CHDTPA.
- CH-DTPA, could effectively remove uranium over a wide pH range of 3-7. Thus, the ideal pH for this investigation was taken to be 7.
- Pseudo-second-order kinetic and Langmuir isotherm models provided the best fit for the adsorption data. At pH 7, CH-DTPA has a maximum adsorption capacity of 2500.0 mg/g, which is the highest reported at neutral pH till date.
- FTIR, XPS and XRD analyses confirmed that uranium bound with CH-DTPA through uranium-amino group chelation and complexation with oxygen and the formation of UO_2 and U_3O_8 species on CHDTPA.
- It was concluded that, the adsorption sites on CH-DTPA were uniform leading to a monolayer adsorption with chemisorption to be limiting step in adsorption of uranium that involved valent force through electron exchange between CH-DTPA, adsorbate, complexation or chelation because the calculated q_e value was very close to the Exp. q_e value.
- The adsorption capacity of CH-DTPA was reduced to about 40-60% in the presence of bicarbonate and carbonate ions and there was no significant interference by other ions such as nitrate, sulphate and chloride.
- Up to four cycles of recycling and reuse were examined, wherein CH-DTPA retained 75% of its efficiency during the 4^{th} cycle.

Chapter 3B

Synthesis of Biochar from Watermelon Rind for Removal of Uranium from Aqueous Solution

3B.1.Materials and Methodology

3B.1.1. Materials and chemicals: Watermelon rind (WMR) was obtained from the girls' hostel at The Maharaja Sayajirao University of Baroda in Vadodara, Gujarat, India. Uranyl Nitrate Hexahydrate puriss AR ($N_2O_8U.H_2O$) which was purchased from Spectrochem PVT.LTD. All chemicals were used as received without any further purification.

3B.1.2 Synthesis of adsorbent: Watermelon rind biochar was synthesized utilizing a previously published technique (Sadhu et al., 2021). The watermelon rind (WMR) was cleaned and dried in the sun till water evaporated, further these were then dried for 24 hours at 100^0C in an oven before being crushed to a fine powder. The fine powder was pyrolyzed in a muffle furnace at 300^0C and 400^0C (at a rate of 10^0C/minute) for 4 hours. The final biochar was thoroughly washed with hot water before being dried at 100^0C and were labeled 3WMB and 4WMB respectively. The formed biochar was characterized both pre and post adsorption using the characterization techniques mentioned in 3.2 section of this chapter 3.

3B.1.3. Proximate analysis WMR and 4WMB: Proximate analysis was conducted using the standard method used by (Guilhen et al., 2019). About 2 g of fresh watermelon peels was weighed in a porcelain crucible and dried in an oven at 100°C to determine the moisture content (MC). The sample was weighed once again after cooling in a desiccator at ambient temperature and the moisture content was calculated using **Equation (3B.1)**:

$$MC\ (\%) = 100 \times [(M_1 - M_2)/M_1] \qquad \textbf{(3B.1)}$$

Where, M_1 is the mass of the watermelon peel and M_2 is the mass of the watermelon peel after oven drying.

The final yield (FY) of biochar of recovered biochar was calculated according to **Equation (3B.2).**

$$FY\ (\%) = 100 \times (M_3/M_2) \qquad \textbf{(3B.2)}$$

Where, M_3 is the mass of the pyrolyzed biochar.

3B.2.Uranium adsorption studies

The uranium adsorption studies were carried out as described in **section 3.3** of this chapter.

3B.3.Results and Discussion

3B.3.1. Proximate analysis: The results of the proximate analysis of the WMPR and 4WMB obtained after oven drying and pyrolysis are shown in **Table 3B.1**. After drying in a hot air oven at 100ºC, the moisture content (MC) of the wet watermelon rind was found to be 93.75% of its entire weight. After pyrolysis at 400°C, the final yield (FY) of the watermelon rind was reported to be 17.2% of the total dry weight.

Table 3B.1. Proximate parameters of watermelon rind.

MC (%) in WMPR	FY (%) of 4WMB
93.75	17.2

3B.3.2.Uranium adsorption studies:

3B.3.2.1.Effect of pH on the adsorption of uranium: The capacity of 4WMB to adsorb uranium in solutions of various pH s (pH = 2, 3, 4, 5, 6, 7, 8, and 10) was examined (other adsorption parameters Ci=30 mg/L, dose=50mg/25mL, time 3 h.). It is evident from **Figure 3B.1(a)** that the adsorption process is pH dependent. The adsorption capacity of 4WMB for uranium increased from 64.35% to 98.09% when the pH of the solution was increased from 2 to 3 and dropped sharply to 69.92% at pH 4. Adsorption was not favored at very low pH levels because of competitive adsorption of UO_2^{2+} and H^+ ions (Corrêa et al., 2015). The interaction between cationic uranium species in solution, such as $(UO_2)_2(OH)_2^{2+}$, UO_2OH^+, $(UO_2)_2OH^{3+}$, $(UO_2)_3(OH)^{5+}$, and $(UO_2)_4(OH)^{7+}$, and the functionalities present on the surface of 4WMB were favored at pH 3 (Mishra et al., 2017; Mustafa et al., 2016).

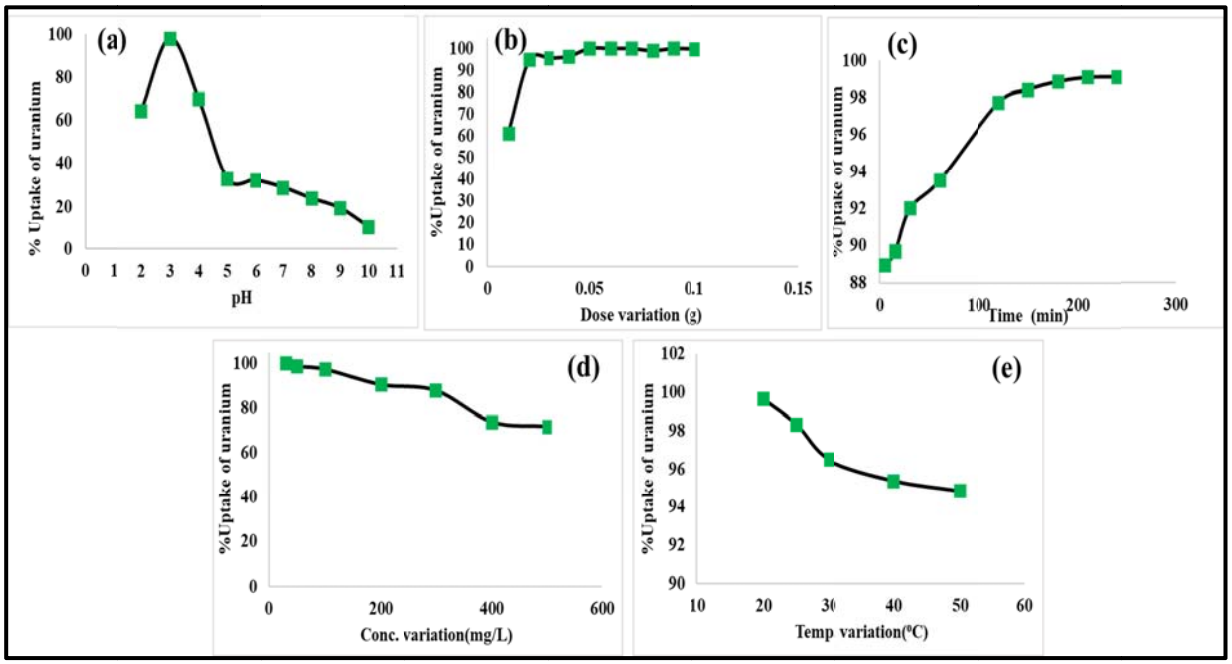

Fig. 3B.1. Adsorption of Uranium **(a)** effect of pH **(b)** effect of dosage **(c)** effect of contact time **(d)** effect of concentration and **(e)** effect of temperature

3B.3.2.2.Effect of adsorbent Dosage on uranium adsorption: Batch sorption experiments with various doses of 4WMB have been carried out to assess the effect of adsorbent dosage on the effectiveness of uranium adsorption using 25 mL of 30 mg/L uranium-containing solution. As seen in **Figure 3B.1(b)** it was found that uranium removal increased with an increase in dosage of 4WMB up to 0.02g as there were more active sites available. However, as the dose was increased further, adsorption remained nearly constant due to the aggregation of adsorption sites, which reduced the total amount of adsorbent surface area that was available to the adsorbate and extended the diffusion path (Ding et al., 2018). An optimum dose of 0.02g was selected for further studies.

3B.3.2.3. Effect of contact time on the adsorption of uranium: Figure 3B.1(c) shows removal of uranium vs contact time for 30 mg/L uranium. Experiments were conducted by equilibrating 25 mL of 30 mg/L uranium solution at pH 3 with 0.02 g of 4WMB for various time periods (5 to 240 minutes), to optimize the impact of contact time. When an equilibrium period was attained, the uranium adsorption increased as the contact time increased and stayed nearly constant. Although a significant amount of uranium (>90%) was eliminated in the first 30 minutes and then increased until equilibrium was achieved in 180 minutes as a result of the initial solute high concentration gradient and availability of adsorption sites

(Ahmed et al., 2021). Thus, 3 hours was chosen as the optimum equilibration time for further study.

3B.3.2.4.Effect of concentration on the adsorption of uranium: The effect of concentration on the adsorption process, ranging from 30 mg/L to 500 mg/L under optimized adsorption conditions, was examined and is depicted in **Figure 3B.1(d)**. It was demonstrated that uranium uptake decreased due to non-availability of active sites (Ahmed et al., 2021).

3B.3.2.5. Effect of temperature on the adsorption of uranium: Figure 3B.1.(e) illustrates how temperature affects the uptake of uranium. Adsorption was an exothermic process since it gradually reduced as the temperature increased. The molecules' greater propensity to escape off the adsorbent surface and into the solution phase, which results in the boundary layer's thickness decreasing, maybe the source of the lower adsorption (Albayari et al., 2021).

3B.3.2.6. Adsorption isotherms: Langmuir and Freundlich's isotherms were used to further model the experimental data. The results of fitting the experimental data to these two models and the sorption parameters are shown in **Table 3B.2 and Figure 3B.2**

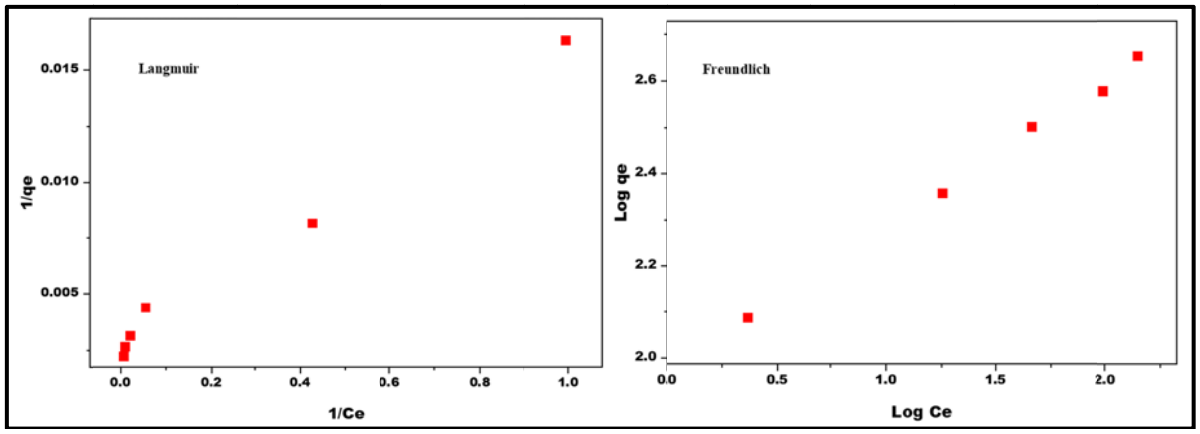

Fig. 3B.2. Isotherms of uranium uptake by 4WMB at pH= 3, dose=0.8gm/L, equilibration time 3 h

Table 3B.2. Isotherm parameters of Langmuir and Freundlich for the adsorption of uranium by WMB

Adsorbent	Freundlich isotherm			Langmuir isotherm			
	1/n	K_f	R^2	q_{max} (mg/g)	K_L (dm^3/mg)	R_L	R^2
4WMB	0.370	73.45	0.972	370.37	0.199	0.092	0.991

The Langmuir model exhibited a better fit than the Freundlich model (R^2= 0.991 vs 0.972), revealing the fact that adsorption process here was mainly taking place on the homogeneous

surface (Liao et al., 2022c). The comparison of the adsorption capacity of 4WMB and the various adsorbents reported in the literature for uranium has been summarized in **Table 3B.3**. In terms of the cost of the material synthesis process and adsorption capacity, 4WMB was found to be a better adsorbent than previous reported ones.

Table 3B.3. Comparison of Adsorption Capacities of various biochar and modified biochar adsorbents for uranium removal

Sr.No.	Materials	pH	Pyrolysis temp. (^{0}C)	Q_{max} (mg/g)	References
1	Switchgrass biochar	3.9	300	4.0	(Kumar et al., 2011)
2	Activated biochar fibers from Opuntia Ficus indica-12M Nitric acid activation	3	600	210	(Hadjittofi and Pashalidis, 2015)
3	Rice straw-based biochars - $KMnO_4$	5.5	550	100	(Yakout, 2016)
4	Eucalyptus biochar	5.5	400	27.2	(Mishra et al., 2017)
5	Biochar fibers derived from Luffa cylindrica sponges- Nitric acid	3	650	92	(Liatsou et al., 2017)
6	WH (Wheat straw) biochar	4.5	450	8.7	(Jin et al., 2018)
7	CW (Cow dungs)			64.0	
8	WH-AO - Nitric acid			355.6	
9	CW-AO- Nitric acid			73.3	
10	Nonmagnetic rice husk biochars	7	500	48.6	(Wang et al., 2018)
11	Magnetic rice husk biochars - $FeSO_4 \cdot 7H_2O$ and NaOH			53.2	
12	Hydrophyte biomass (magnetic biochar)- $FeCl_2 \cdot 4H_2O$	3	700	54.35	(Hu et al., 2018b)
13	Wheat straw biochar (WS)	5-6	550	25	(Alam et al., 2018)
14	Bamboo (Acidosasa longigula) shoot shell biochar	4	500	32.3	(Hu et al., 2018a)
15	Fe_3O_4-loaded oxidized biochar (pncom) from pine needles- $FeSO_4 \cdot 7H_2O$ $FeCl_3$	6	600	2.6 mol/kg	(Philippou et al., 2019)
16	Magnetic watermelon rind biochar - $FeCl_3 \cdot 6H_2O$ and $FeSO_4 \cdot 7H_2O$	4	500	323.56	(Lingamdinne et al., 2022)
17	Watermelon rind biochar			135.86	
18	Watermelon rind biochar	3	300	112.36	This study
			400	370.37	

Additionally, the batch adsorption parameters for 3WMB were optimized. With the exception of the maximum adsorption capacity (112.36mg/g), which is significantly lower than that of 4WMB (370.37mg/g), the same optimal conditions were obtained for 3WMB as for 4WMB.

3B.3.2.7. Adsorption thermodynamics: The thermodynamic parameters of the adsorption process were calculated from experimental data collected at different temperatures and a plot

of 1/T versus $\ln K_L$ was obtained using **Equation 3.10** as shown in **Figure 3B.3**. The thermodynamic parameters obtained for the adsorption of uranium on 4WMB, such as change in free energy (ΔG°), enthalpy (ΔH°), and entropy (ΔS°), are reported in **Table 3B.4.** The exothermic and feasible nature of the uranium adsorption on 4WMB at ambient conditions was indicated by the negative value of ΔH^0 (Banerjee et al., 2016). Furthermore, negative values of ΔS^0 indicated a rise in maximum adsorption between 25 and 30° C due to better adsorption of the metal ion. Additionally, it is possible to claim that the inefficiency of the adsorption process at higher temperatures was caused by a change in system enthalpy, which suggested a buildup of heat in the environment and a resultant decrease in the possibility of bond formation and its stability (Chowdhury and Das, 2011). The reaction was feasible at low temperatures.

Table 3B.4. Thermodynamic data of uranium on 4WMB.

Temp.(K)	K_L	ΔS J/K/Mol	ΔH^0 (KJ mol^{-1})	R^2	ΔG^0 (KJ mol^{-1})
25	24.583	-83.53	-32.52	0.928	-7.93
30	15.906				-6.97
40	10.314				-6.07
50	8.657				-5.80

3B.3.2.8. Kinetic studies: The kinetic data of uranium adsorption on 4WMB was assesses using the pseudo 1st and 2nd order rate models **(Equations 3.8 and 3.9, respectively)** were used in this study. The findings of the respective kinetic parameters are given in **Table 3B.5**, along with the fitting of two kinetic models to the uranium equilibrium data (**Figure 3B.3)**. The pseudo-2nd-order kinetics was found to have a better value of the linear regression coefficient ($R^2 > 0.99$) than a pseudo-1st-order model ($R^2 < 0.90$), making it the best-fitted model for describing the kinetics of uranium adsorption on 4WMB. The computed and experimental adsorption capacity (q_e) values coincide rationally, favoring the pseudo-2nd order kinetic model. The aforementioned findings demonstrated that the concentrations of the biosorbent and uranium were responsible for the rate-determining step during uranium binding on the 4WMB. Additionally, this suggested that uranium was adsorbed on biochar by a chemisorption method (Siddiqui et al., 2020).

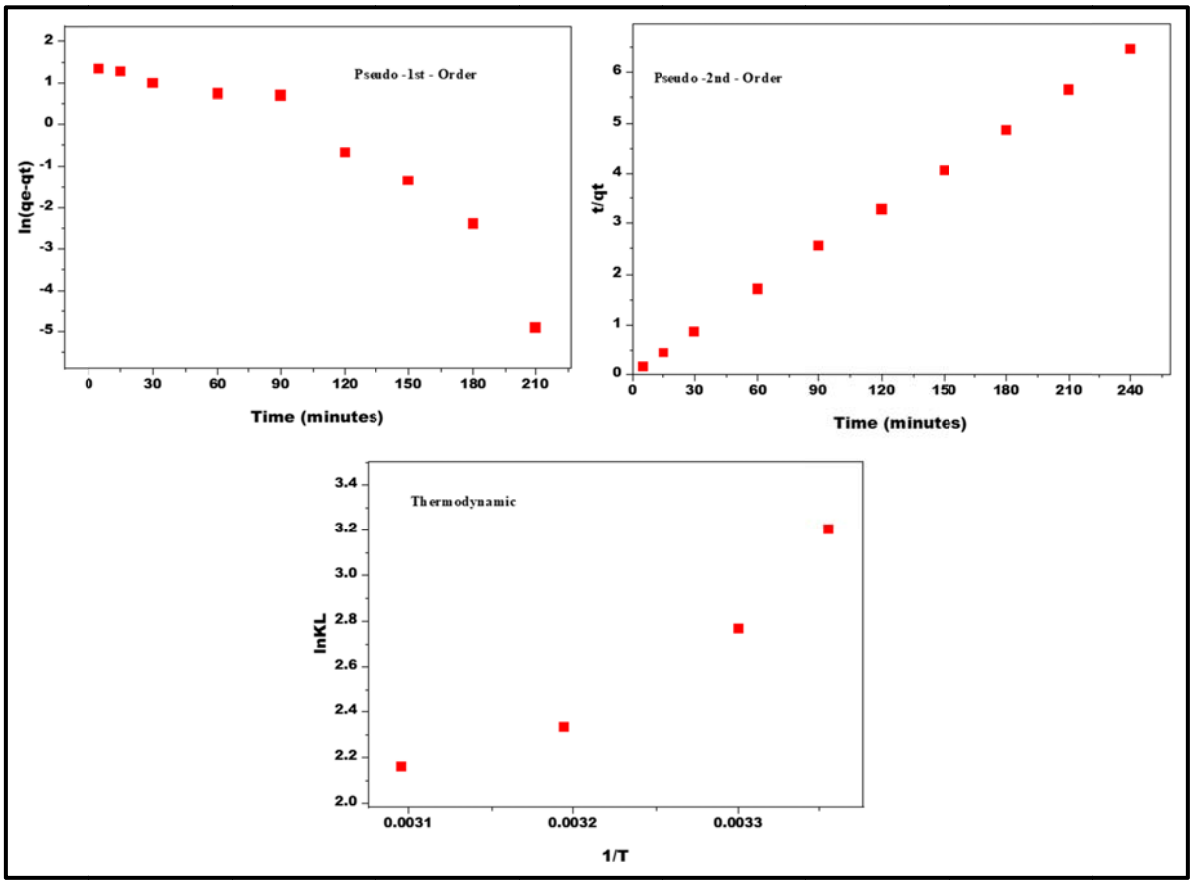

Fig. 3B.3. Kinetics and thermodynamic of uranium uptake by 4WMB (circumstances: pH= 3, Ci=30 mg/L, dose=20mg, volume=0.025L)

Table 3B.5. Kinetic parameters of uranium adsorption on 4WMB

Pseudo -1st- order			**Pseudo -2nd - order**			
q_e (mg/g)	**K_1**	**R^2**	**q_e exp**	**q_e (mg/g)**	**K_2**	**R^2**
7.85	-0.00015	0.86	37.17	37.52	0.0099	1.00

3B.3.2.9.Application to groundwater samples and simulated water: The effectiveness of 4WMB in removing uranium from real water samples from the environmental department, MSU, and simulated water (ASTM, 2019) was tested. There was synthesized simulated water using already published literature. **Tables 3A.5 and 3B.6** report the qualities of the groundwater samples and the composition of simulated water respectively. When the collected groundwater sample was analyzed, no detectable level of uranium was identified. The groundwater was spiked with standard uranium solution (20, 30, and 50 mg/L), and an adsorption experiment using 0.8 g/L of 4WMB was conducted with 3 h of contact time at natural pH (7.37). The study showed that only 15% uranium could be removed though

effective at pH 3. The removal of uranium by WMB may include electrostatic interactions and adsorption as well precipitation on minerals as uranium oxide, hydroxide and carbonate at higher concentrations (Liao et al., 2022b).

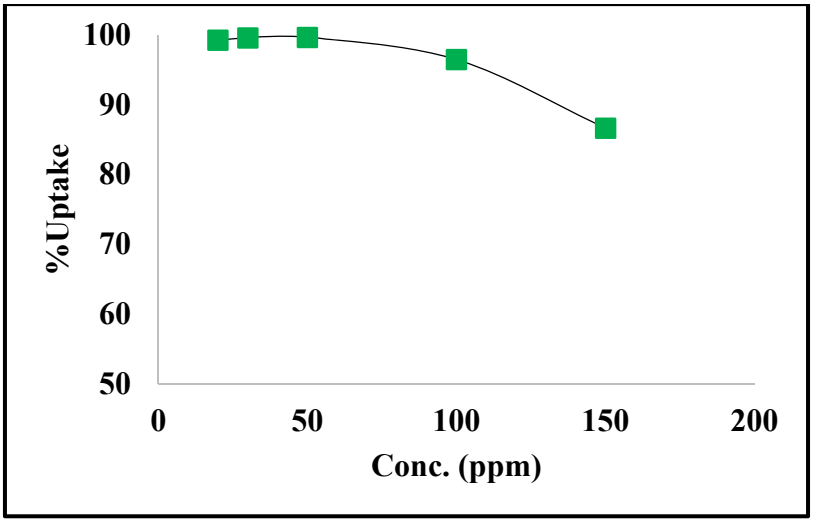

Fig. 3B.4. Removal of uranium from simulated water (pH: 3, dose:20mg, volume:0.025L, time:3h)

Simulated seawater was prepared in the lab using the reported method (ASTM, 2019). A spike of standard uranium solution (20, 30, 50, 100, and 150 mg/L) was added to the simulated seawater, and an adsorption experiment was carried out with 20mg of adsorbent for 0.025L, at pH 3 with 3h of contact time. It may be observed that up to 87%.of 150mg/L uranium was effectively removed **(Figure 3B.4).**

Table 3B.6. Composition of simulated seawater

Sodium chloride (NaCl)	24.53g/L
Magnesium chloride ($MgCl_2$)	5.20g/L
Sodium sulfate (Na_2SO_4)	4.09g/L
Calcium chloride ($CaCl_2$)	1.16g/L
Potassium chloride (KCl)	0.695g/L
Sodium bicarbonate ($NaHCO_3$)	0.201g/L
Potassium bromide (KBr)	0.101g/L
Boric acid (H_3BO_3)	0.027g/L
Strontium chloride ($SrCl_2$)	0.0025g/L
Sodium fluoride (NaF)	0.003g/L
Water (H_2O)	988.968g/L
Total	1025g/L

3B.3.2.10. Reusability and effect of electrolytes on uranium adsorption by 4WMB: The desorption of uranium ions adsorbed onto 4WMB was investigated with 0.1M, 0.5 M and 1M NaOH, HCl and Na_2CO_3 solutions. It was observed that maximum desorption was achieved with 0.1M NaOH which was further utilized for desorption of CH DTPA which was equilibrated with 30mg/L of uranium to carry out the reusability of the adsorbent. 0.1M NaOH solution was used for the desorption to evaluate the reusability of the adsorbent. The adsorbent was dried and utilized again for the adsorption process after desorption. In the first, second, third, and fourth cycles of batch operations, the percentage of uranium uptake was determined to be 100%, 94.94%, 79.96%, and 71.31%, respectively **(Figure. 3B.5a)**. The outcome demonstrates the adsorbent's high sustainability for industrial or commercial use.

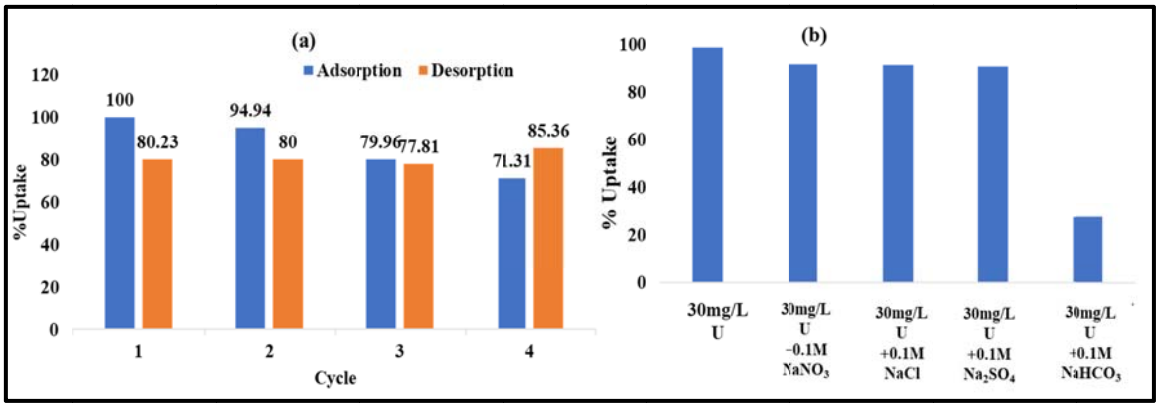

Fig. 3B.5. (a) % removal of uranium after consecutive 1st 2nd 3rd and 4th cycles and **(b)** effect of electrolytes on % uptake of uranium.

Considering potential electrolytes that could be present in water samples, such as $NaNO_3$, NaCl, Na_2SO_4, and $NaHCO_3$ which could change the electrostatic interaction between the 4WMB surface and uranium ion, their impact on uranium adsorption at a concentration of 0.1M was examined. According to the findings in **Figure 3B.5b**, the presence of NaCl, $NaNO_3$, and Na_2SO_4 had very little impact on uranium adsorption. The percentage of uranium adsorption has, however, significantly decreased in the case of $NaHCO_3$ due to complexation with uranium. There was no interference up to 145 mg/L of bicarbonate on the uptake of uranium by 4WMB as indicated by simulated water, groundwater and effect of electrolytes.

3B.4.Characterization of adsorbent before (4WMB) and after adsorption of uranium (4WMBU)

3B.4.1. FTIR: FTIR spectral analyses of 4WMB before and after uranium adsorption are shown in **Figure 3B.6.** The symmetric and asymmetric C-H stretching of the aliphatic vibrational groups was observed in the range of 2980-2800 cm^{-1} indicating that the cellulose was not entirely carbonized at 400°C (Guilhen et al., 2019). The peaks at about 2347 cm^{-1} corresponded to ketone or ketene, and the peaks at 1556 and 1576 cm^{-1} was attributed COO– asymmetric stretching. The peaks at 1269 and 1281 cm^{-1} can be ascribed to the O–H stretching of phenolic compounds. Other peaks that can be seen include the peaks at 1580 to 1590 cm^{-1} which can be attributed to the COO– asymmetric stretching, the peak at 1457 cm^{-1} corresponded to C–H deformation of CH_3 groups, the 1065 cm^{-1} corresponding to the straight chain C–C stretching or C–OH stretching, a weak band at 746 cm^{-1} can be seen which is attributed to the aromatic C-H band suggesting a condensed structure formation. The peak at 562 cm^{-1} that shifted to 544 cm^{-1} in uranium loaded biochar was attributed to metal-O stretching. The new peaks at 1729.36 cm^{-1} can be attributed to binding of uranium to carboxyl group and the peaks at 1462.53 cm^{-1} and 1124 cm^{-1} corresponded to the C=C and C-O stretching respectively, indicate the presence of uranium on 4WMB.

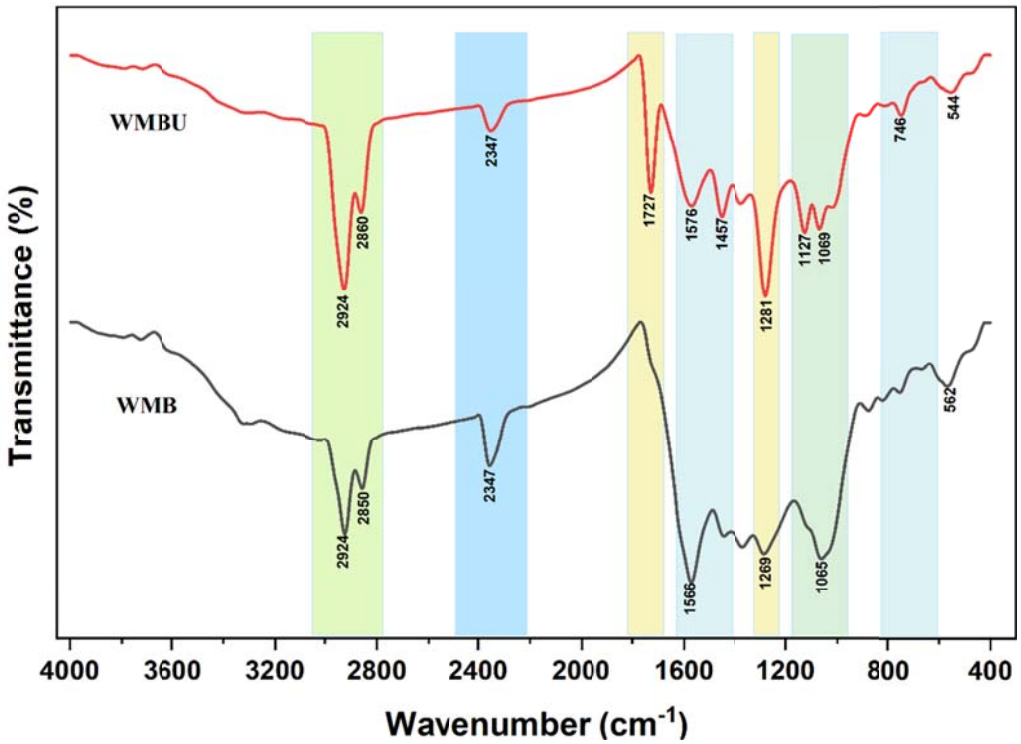

Fig. 3B.6. IR spectra of pristine (4WMB) and loaded with uranium (4WMBU)

3B.4.2. TGA: The thermogram of the adsorbent before and after uranium adsorption is shown in **Figure 3B.7(a)&(b).** The temperature was increased from 30 to 560°C at a rate of 10 °C per minute while a sample weighing 5–10 mg was placed in the sample pan. The TGA showed the first weight loss of 21.84% and 11.46% in 4WMB and 4WMBU respectively at approximately 100°C. This weight loss may have been caused by the physical adsorption of water and loss of moisture content. Weight loss resulting from the breakdown of cellulosic and hemicellulosic components was observed at ~400°C both before and after uranium adsorption on 4WMB. The 2nd weight loss of 11.41% and 10.41% was caused by the degradation of lignin, which happens around 500°C (Hernandez-Mena et al., 2014). When the temperature reached 560°C, there was no discernible weight loss due to the residue and crystals such as calcites and quartz along with fixed carbon. The presence of uranium as stable oxide has lower weight loss in 4WMBU.

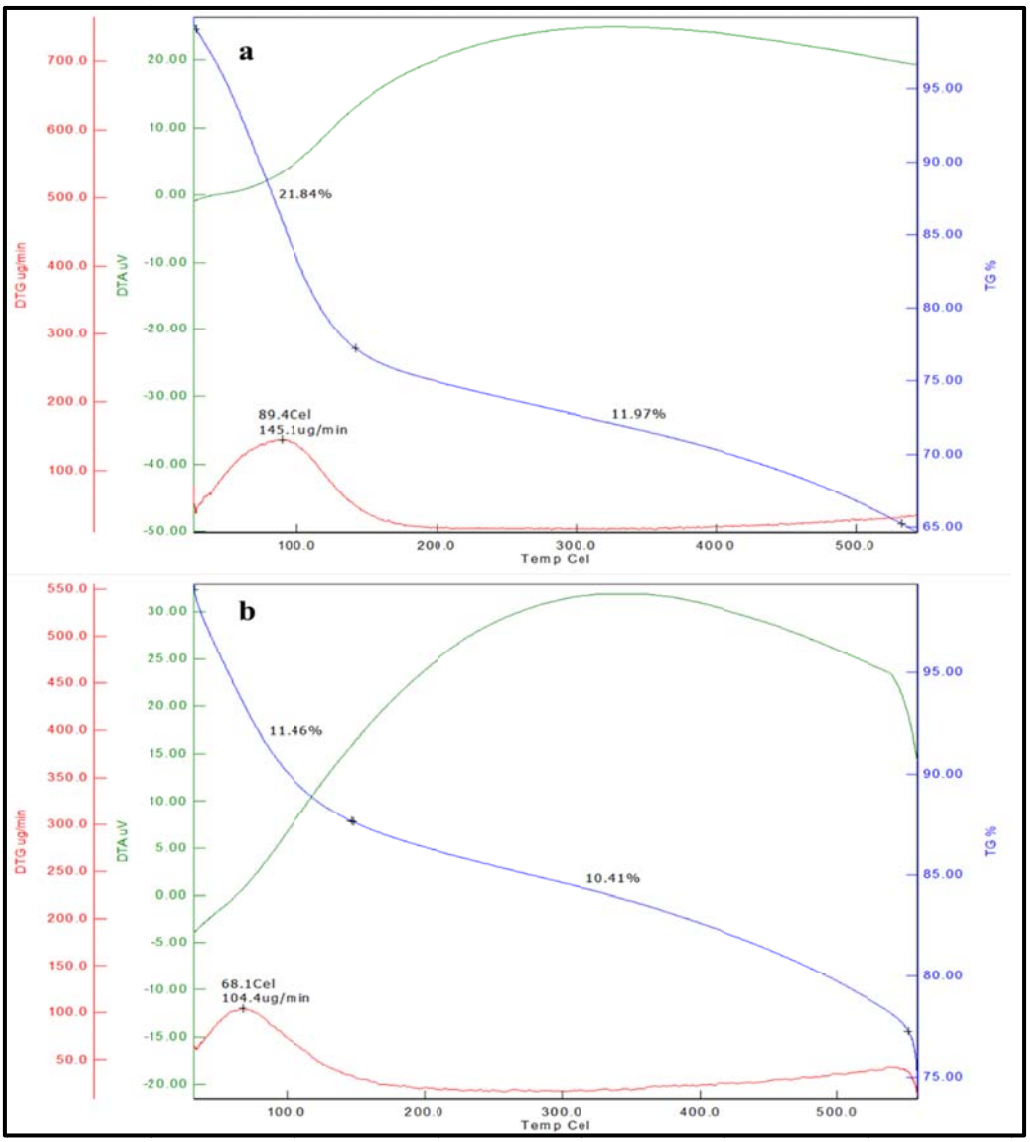

Fig.3B.7.TGA spectra of **(a)** 4WMB and **(b)** 4WMBU

3B.4.3.BET: The BET analysis was performed for both pre- and post-uranium adsorption 4 WMB samples in order to determine the material's specific surface areas and pore size distributions. The surface area of the material increased from 1.705 m^3/g to 4.239 m^3/g after uranium was adsorbed on the adsorbent, average pore diameters of 134.785 Å and 133.438 Å for 4WMB and 4WMBU, respectively. With adsorption of uranium into the pores there might be a change in pore framework leading to change in surface morphology.

3B.4.4.XRD: XRD spectra demonstrated the amorphous nature of biochar, as seen in **Figure 3B.8** by the broad peak between 20° to 30° due to disordered carbon (Tran et al., 2015; Zheng et al., 2020). The XRD spectrum of biochar after adsorption of uranium indicated U_3O_8 phase (PDF no. 31-1424) and clarkelite (PDF no. 50-1586).

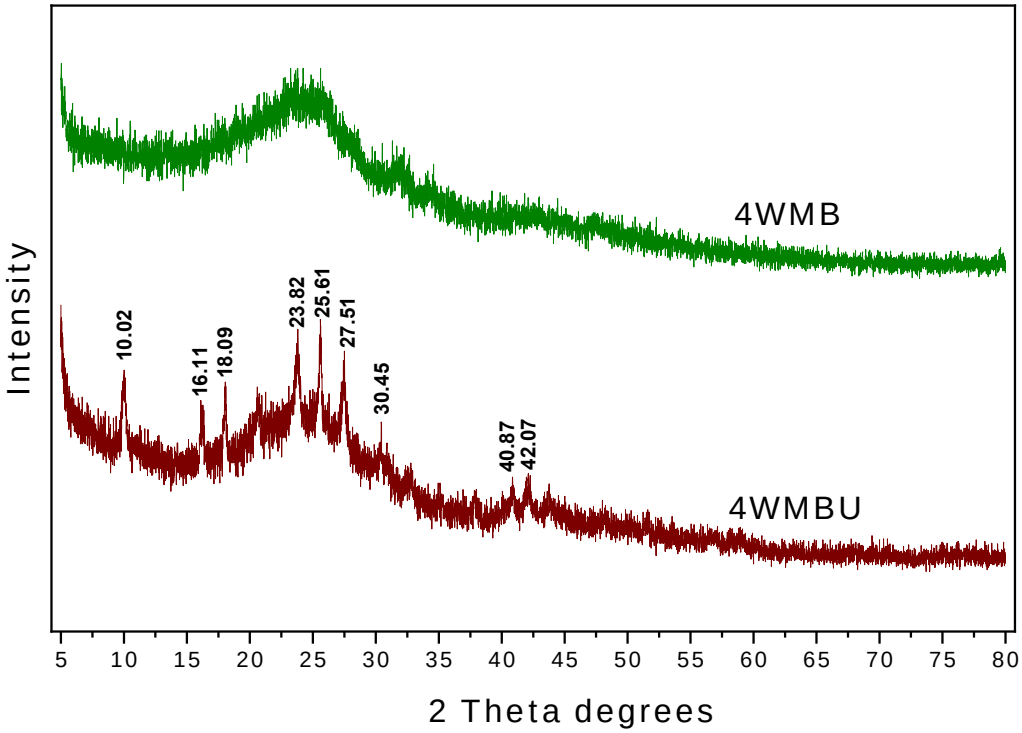

Fig.3B.8. XRD graphs of 4WMB and 4WMBU.

3B.4.5. SEM-EDX: SEM and EDX methods were used to characterize the surface elements and microstructure of the 4WMB adsorbent both before and after uranium adsorption **(Figure 3B.9 a&b**). After uranium adsorption, the amounts of Mg, Ca, Si, K, and P on the surface of biochar decreased and presence of U was observed. The ion exchange of U at these sites may be the reason for the elemental decrease. As can be seen in **Figure 3B.9 4c&d**, the adsorbent surface pore structure diminished and a change in morphology to a fibrous needle was

observed as a result of the adsorption of uranium. The results of the BET analysis aligned with these findings.

3B.4.6. XPS: As seen in **Figure 3B.10(a)** The XPS spectra of the adsorbent revealed significant carbon and oxygen peaks prior to uranium adsorption, which remained prominent even after uranium adsorption. The $4f_{5/2}$ signal at 392.82 eV and $4f_{7/2}$ signal at 381.99 eV with satellites at 384.8 and 390.6 eV as shoulders was assigned to U(VI) as seen in **Figure 3B.10(b).** The atomic % of 4WMB for O1s, N1s, C1s were 35.12%, 6.234% and 58.64% respectively and in case of 4WMBU, these were 31.32%, 4.021%, 40.98%, respectively along with 24.3% of U4f.

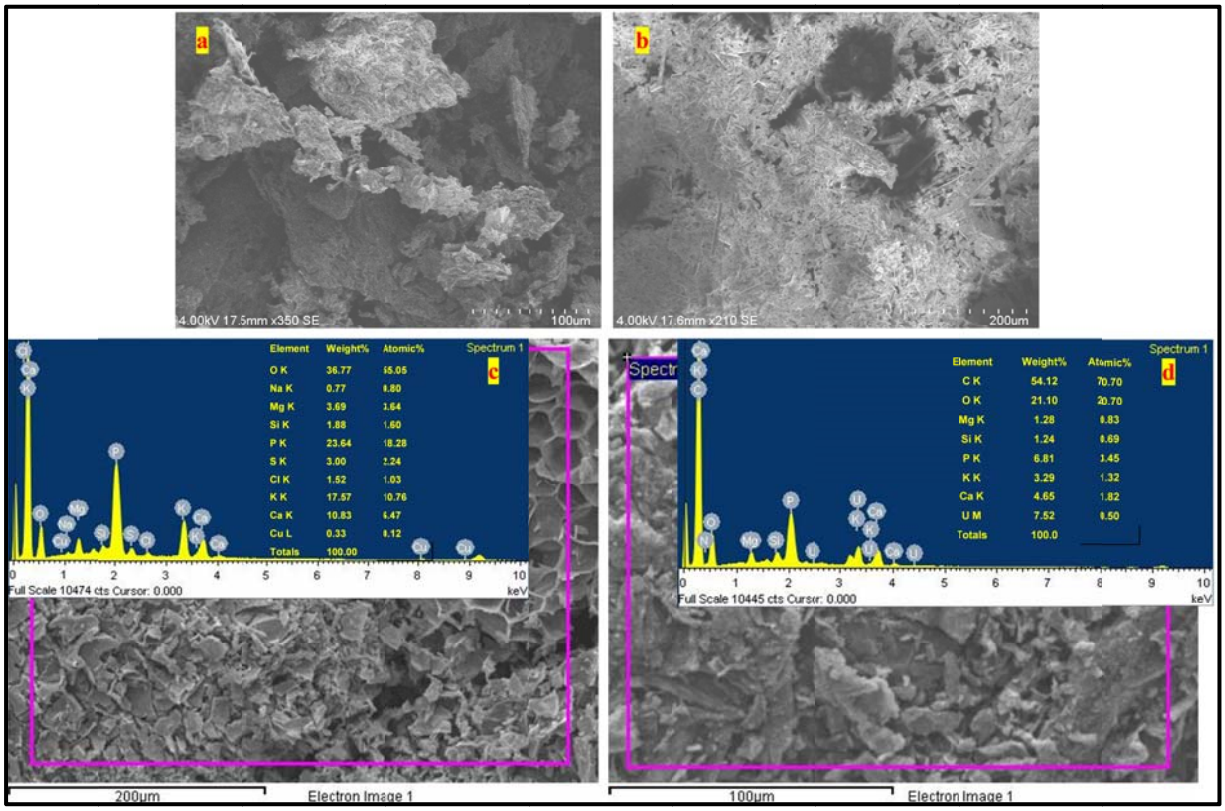

Fig.3B.9.SEM images of **(a)** 4WMB and **(b)** 4WMBU, **(c)** EDX spectra of 4WMB **(d)** EDX spectra of 4WMBU

Further as seen in **Figure 3B.10(c&d)** the deconvoluted spectra of C1s and O1s were plotted for 4WMB. Post adsorption the deconvoluted spectra of C1s and O1s were plotted for 4WMBU **(Figure 3B.10 e&f)** and it could be seen that there was a shift in the peaks post adsorption suggestive of binding of uranium to the adsorbent. As seen in the **Figure 3B.12(c)**

the peaks at 285.07 eV can be attributed to C=C and the peak at 285.9 eV to the C-O bond. After adsorption of Uranium the peaks for C=C and C-O shifted to the 284.36 eV and 286.06 eV respectively **(Figure 3B.10(e))** suggesting the binding of uranium with the functional groups of the biochar. Similarly, shifts are seen in the O1s spectra before and after adsorption, where the peak at 530.69 eV **(Figure 3B.10(d))** is seen at 532.42 eV **(Figure 3B.10(f))** again suggestive of the effective binding of the oxygen containing functional groups of biochar to uranium.

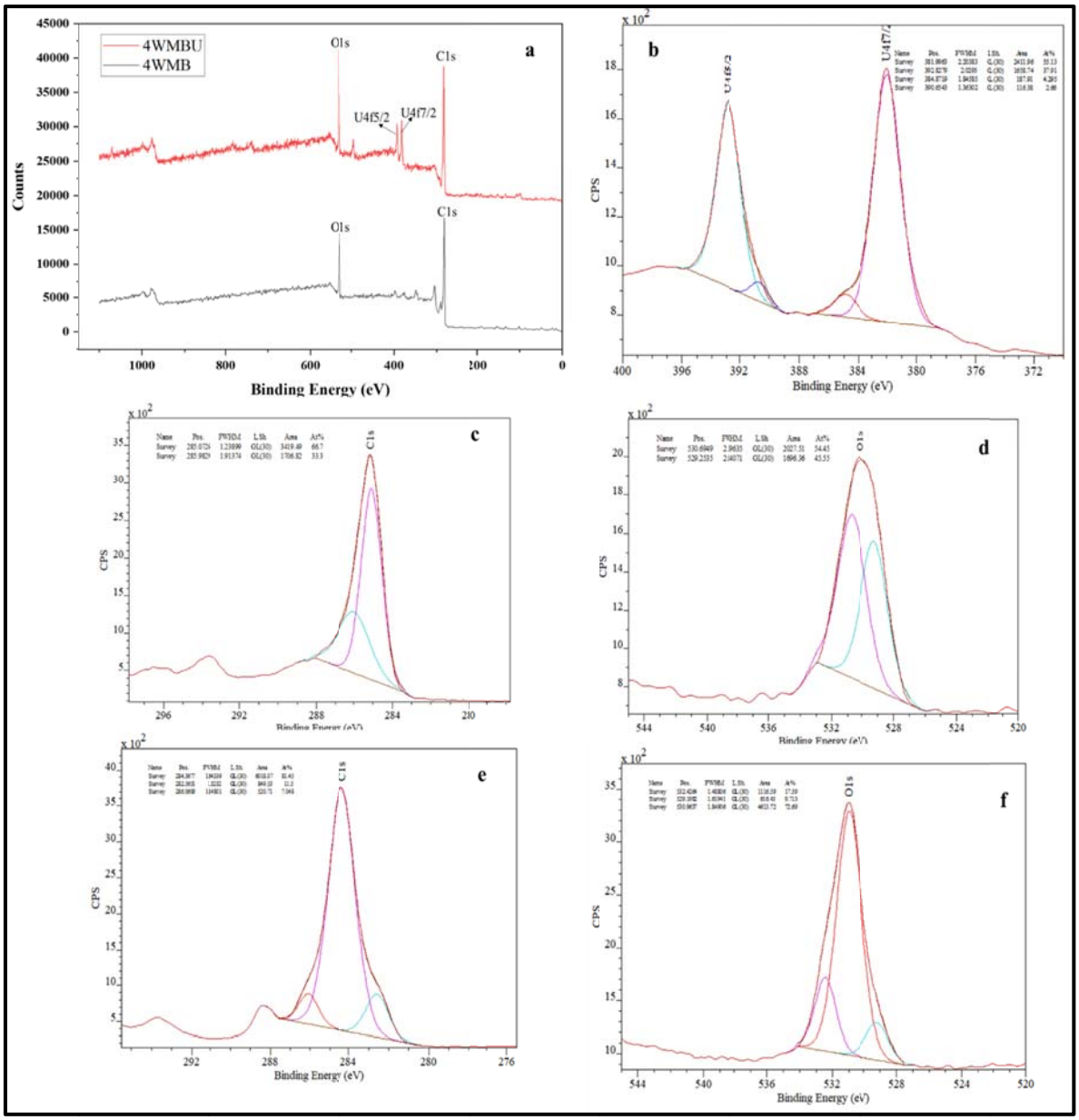

Fig.3B.10. XPS spectra depicting **(a)** survey spectra of 4WMB and 4WMBU, **(b)** deconvolution of the peak U4f in 4WMBU, **(c&d)** deconvoluted spectra of Carbon and Oxygen in 4WMB, **(e&f)** XPS peaks of carbon and oxygen 4WMBU respectively.

Ion exchange, surface complexation, electrostatic attraction, and precipitation are a plausible uranium adsorption mechanism (Huang et al., 2024). It is evident from EDS and XRD methods that 4WMB contains calcium, potassium, and magnesium ions. Accordingly, uranium can be effectively adsorbed on the adsorbent by these ions via an ion exchange mechanism. **Figure.3B.11** shows a plausible mechanism of uranium adsorption on 4WMB.

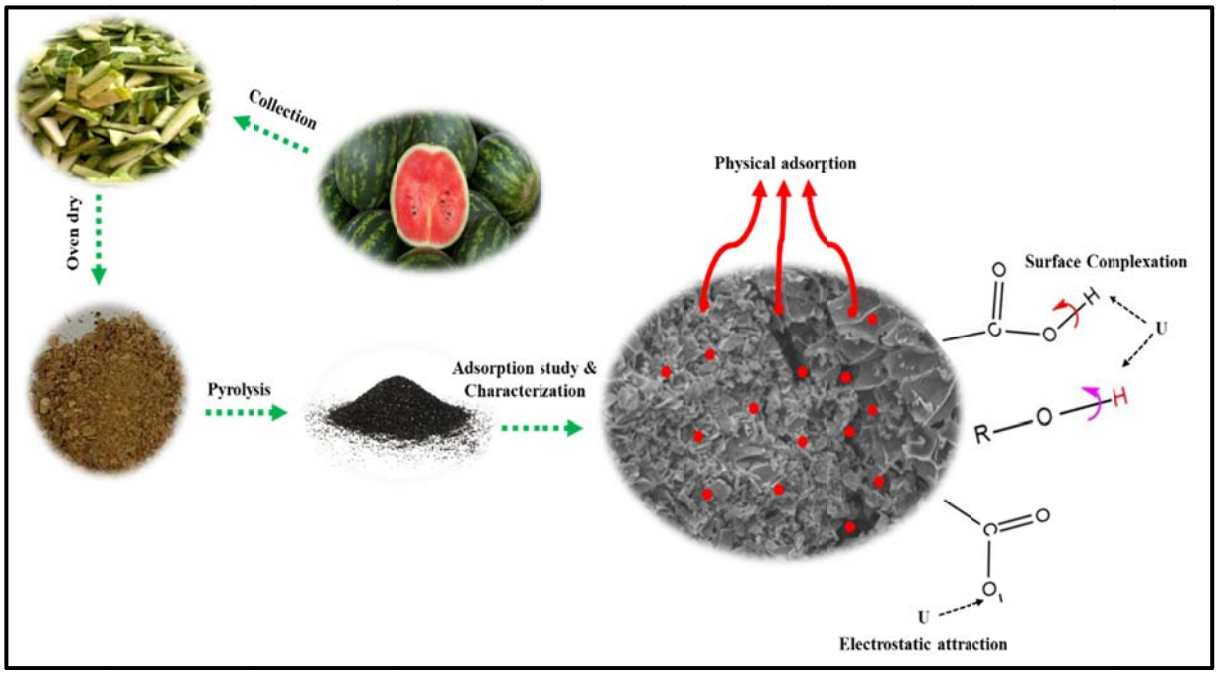

Fig.3B.11. Plausible adsorption mechanism of uranium on 4WMB

Conclusion

- 4WMB was characterized by FTIR, TGA, BET, SEM-EDS, XRD and XPS techniques. FTIR and XPS suggested the presence of condensed aromatic structures with functional groups such as carboxyl groups and keto groups were responsible for uranium binding with 4WMB.
- The initial pH, uranium concentration, and temperature had a significant impact on the uranium's adsorption capacity to bind with 4WMB.
- The Langmuir isotherm and pseudo-second-order kinetic models fit the experiment results well. Under ideal conditions (pH 3, contact period 180 minutes, 0.8 g/L biosorbent dose, room temperature, 30mg/L uranium conc.), the maximum adsorption capacity of 4WMB was 370.37 mg/g which was comparable to biochars reported in literatures. It was observed that uranium adsorption on 4WMB decreased with increasing temperature.

- The adsorption data could be best fitted to Langmuir isotherm model and Pseudo -2nd- order models indicative of chemisorption as a monolayer.
- The best desorption agent for removing the adsorbed uranium from 4WMB was found to be 0.1M NaOH.
- Characterization of 4WMBU indicated that adsorption of uranium effectively occurred by chemisorption at C=O functionalities and formed U_3O_8 and clarkelite uranium species as indicated by XRD and XPS confirmed the presence of U (VI) species.
- It has been found that 4WMB can effectively remove up to 87% of 150 mg/L of uranium ion from simulated sea water at optimal pH of 3.

References

Abney CW, Mayes RT, Saito T, Dai S. Materials for the Recovery of Uranium from Seawater. Chemical Reviews 2017; 117: 13935-14013.

Adhikari S, Timms W, Mahmud MAP. Optimising water holding capacity and hydrophobicity of biochar for soil amendment – A review. Science of The Total Environment 2022; 851: 158043.

Ahmed W, Núñez-Delgado A, Mehmood S, Ali S, Qaswar M, Shakoor A, et al. Highly efficient uranium (VI) capture from aqueous solution by means of a hydroxyapatite-biochar nanocomposite: Adsorption behavior and mechanism. Environmental Research 2021; 201: 111518.

Alam MS, Gorman-Lewis D, Chen N, Safari S, Baek K, Konhauser KO, et al. Mechanisms of the Removal of U(VI) from Aqueous Solution Using Biochar: A Combined Spectroscopic and Modeling Approach. Environmental Science & Technology 2018; 52: 13057-13067.

Albayari M, Nazal MK, Khalili FI, Nordin N, Adnan R. Biochar derived from Salvadora persica branches biomass as low-cost adsorbent for removal of uranium(VI) and thorium(IV) from water. Journal of Radioanalytical and Nuclear Chemistry 2021; 328: 669-678.

Anirudhan TS, Lekshmi GS, Shainy F. Synthesis and characterization of amidoxime modified chitosan/bentonite composite for the adsorptive removal and recovery of uranium from seawater. Journal of Colloid and Interface Science 2019; 534: 248-261.

Anirudhan TS, Rijith S. Synthesis and characterization of carboxyl terminated poly(methacrylic acid) grafted chitosan/bentonite composite and its application for the recovery of uranium(VI) from aqueous media. Journal of Environmental Radioactivity 2012; 106: 8-19.

ASTM. Artificial Seawater" ASTM D1141-98. Lake Products Company LLC, USA, 2019.

Ayub A, Raza ZA, Majeed MI, Tariq MR, Irfan A. Development of sustainable magnetic chitosan biosorbent beads for kinetic remediation of arsenic contaminated water. International Journal of Biological Macromolecules 2020; 163: 603-617.

Banerjee S, Mukherjee S, LaminKa-ot A, Joshi SR, Mandal T, Halder G. Biosorptive uptake of Fe^{2+}, Cu^{2+} and As^{5+} by activated biochar derived from Colocasia esculenta: Isotherm, kinetics, thermodynamics, and cost estimation. Journal of Advanced Research 2016; 7: 597-610.

Bera S, Sali SK, Sampath S, Narasimhan SV, Venugopal V. Oxidation state of uranium: an XPS study of alkali and alkaline earth uranates. Journal of Nuclear Materials 1998; 255: 26-33.

Bhatt R, Sreedhar B, Padmaja P. Adsorption of chromium from aqueous solutions using crosslinked chitosan–diethylenetriaminepentaacetic acid. International Journal of Biological Macromolecules 2015; 74: 458-466.

Chi NTL, Anto S, Ahamed TS, Kumar SS, Shanmugam S, Samuel MS, et al. A review on biochar production techniques and biochar based catalyst for biofuel production from algae. Fuel 2021; 287: 119411.

Chowdhury S, Das P. Adsorption Thermodynamics and Kinetics of Malachite Green onto Ca(OH)2-Treated Fly Ash. Journal of Environmental Engineering 2011; 137: 388-397.

Christou C, Philippou K, Krasia-Christoforou T, Pashalidis I. Uranium adsorption by polyvinylpyrrolidone/chitosan blended nanofibers. Carbohydrate Polymers 2019; 219: 298-305.

Corrêa WC, Guilhen SN, Ortiz N, Fungaro DA. Evaluation of adsorption of uranium from aqueous solution using biochar materials. 2015.

Ding L, Tan W-f, Xie S-b, Mumford K, Lv J-w, Wang H-q, et al. Uranium adsorption and subsequent re-oxidation under aerobic conditions by Leifsonia sp. - Coated biochar as green trapping agent. Environmental Pollution 2018; 242: 778-787.

Ebisike K, Elvis Okoronkwo A, Kanayo Alaneme K, Jeremiah Akinribide O. Thermodynamic study of the adsorption of Cd2+ and Ni2+ onto chitosan – Silica hybrid aerogel from aqueous solution. Results in Chemistry 2023; 5: 100730.

Freundlich H. Over the adsorption in solution. J. Phys. chem 1906; 57: 1100-1107.

Galhoum AA, Mahfouz MG, Gomaa NA, Abdel-Rehem SS, Atia AA, Vincent T, et al. Cysteine-Functionalized Chitosan Magnetic Nano-Based Particles for the Recovery of Uranium(VI): Uptake Kinetics and Sorption Isotherms. Separation Science and Technology 2015; 50: 2776-2789.

Gopinath A, Divyapriya G, Srivastava V, Laiju AR, Nidheesh PV, Kumar MS. Conversion of sewage sludge into biochar: A potential resource in water and wastewater treatment. Environmental Research 2021; 194: 110656.

Guilhen S, Masek O, Ortiz N, Izidoro J, Fungaro D. Pyrolytic temperature evaluation of macauba biochar for uranium adsorption from aqueous solutions. Biomass and Bioenergy 2019; 122.

Hadjittofi L, Pashalidis I. Uranium sorption from aqueous solutions by activated biochar fibres investigated by FTIR spectroscopy and batch experiments. Journal of Radioanalytical and Nuclear Chemistry 2015; 304: 897-904.

Hamza MF, Gamal A, Hussein G, Nagar MS, Abdel-Rahman AA-H, Wei Y, et al. Uranium(VI) and zirconium(IV) sorption on magnetic chitosan derivatives – effect of different functional groups on separation properties. Journal of Chemical Technology & Biotechnology 2019; 94: 3866-3882.

Han L, Sun H, Ro KS, Sun K, Libra JA, Xing B. Removal of antimony (III) and cadmium (II) from aqueous solution using animal manure-derived hydrochars and pyrochars. Bioresource Technology 2017; 234: 77-85.

Hernandez-Mena L, Pecora A, Beraldo A. Slow Pyrolysis of Bamboo Biomass: Analysis of Biochar Properties. Chemical Engineering Transactions 2014; 37: 115-120.

Ho Y-S. Review of second-order models for adsorption systems. Journal of hazardous materials 2006; 136: 681-689.

Hu H, Zhang X, Wang T, Sun L, Wu H, Chen X. Bamboo (Acidosasa longiligula) shoot shell biochar: its potential application to isolation of uranium(VI) from aqueous solution. Journal of Radioanalytical and Nuclear Chemistry 2018a; 316: 349-362.

Hu Q, Zhu Y, Hu B, Lu S, Sheng G. Mechanistic insights into sequestration of U(VI) toward magnetic biochar: Batch, XPS and EXAFS techniques. Journal of Environmental Sciences 2018b; 70: 217-225.

Hu X, Zhang X, Ngo HH, Guo W, Wen H, Li C, et al. Comparison study on the ammonium adsorption of the biochars derived from different kinds of fruit peel. Science of The Total Environment 2020; 707: 135544.

Huang F-Y, Dong F, Chen L, Zeng Y, Zhou L, Sun S, et al. Biochar-mediated remediation of uranium-contaminated soils: evidence, mechanisms, and perspectives. Biochar 2024; 6.

Huang G, Peng W, Yang S. Synthesis of magnetic chitosan/graphene oxide nanocomposites and its application for U(VI) adsorption from aqueous solution. Journal of Radioanalytical and Nuclear Chemistry 2018; 317: 337-344.

Huang Y, Zheng H, Li H, Zhao C, Zhao R, Li S. Highly selective uranium adsorption on 2-phosphonobutane-1,2,4-tricarboxylic acid-decorated chitosan-coated magnetic silica nanoparticles. Chemical Engineering Journal 2020; 388: 124349.

Ilton ES, Boily J-F, Bagus PS. Beam induced reduction of U(VI) during X-ray photoelectron spectroscopy: The utility of the U4f satellite structure for identifying uranium oxidation states in mixed valence uranium oxides. Surface Science 2007; 601: 908-916.

Jin J, Li S, Peng X, Liu W, Zhang C, Yang Y, et al. HNO3 modified biochars for uranium (VI) removal from aqueous solution. Bioresource Technology 2018; 256: 247-253.

Kamali M, Sweygers N, Al-Salem S, Appels L, Aminabhavi TM, Dewil R. Biochar for soil applications-sustainability aspects, challenges and future prospects. Chemical Engineering Journal 2022; 428: 131189.

Kant Bhatia S, Palai AK, Kumar A, Kant Bhatia R, Kumar Patel A, Kumar Thakur V, et al. Trends in renewable energy production employing biomass-based biochar. Bioresource Technology 2021; 340: 125644.

Khan MH, Warwick P, Evans N. Spectrophotometric determination of uranium with arsenazo-III in perchloric acid. Chemosphere 2006; 63: 1165-9.

Kumar S, Loganathan VA, Gupta RB, Barnett MO. An Assessment of U(VI) removal from groundwater using biochar produced from hydrothermal carbonization. Journal of Environmental Management 2011; 92: 2504-2512.

Kushwaha S, Sudhakar PP. Adsorption of mercury(II), methyl mercury(II) and phenyl mercury(II) on chitosan cross-linked with a barbital derivative. Carbohydrate Polymers 2011; 86: 1055-1062.

Kushwaha S, Sudhakar PP. Sorption of uranium from aqueous solutions using palm-shell-based adsorbents: a kinetic and equilibrium study. Journal of Environmental Radioactivity 2013; 126: 115-124.

Kyzas GZ, Bikiaris DN. Recent modifications of chitosan for adsorption applications: a critical and systematic review. Mar Drugs 2015; 13: 312-37.

Lagergren SK. About the theory of so-called adsorption of soluble substances. Sven. Vetenskapsakad. Handingarl 1898; 24: 1-39.

Langmuir I. The Constitution and Fundamental Properties of Solids and Liquids. Part I. Solids. Journal of the American Chemical Society 1916; 38: 2221-2295.

Liao J, Chen H, Zhang Y, Zhu W. Pyrolysis of animal manure under nitrogen atmosphere: An environment protection way to obtain animal manure biochar for high-efficient adsorption of uranium (VI). Journal of Analytical and Applied Pyrolysis 2022a; 163: 105493.

Liao J, Ding L, Zhang Y, Zhu W. Efficient removal of uranium from wastewater using pig manure biochar: Understanding adsorption and binding mechanisms. Journal of Hazardous Materials 2022b; 423: 127190.

Liao J, He X, Zhang Y, Zhu W, Zhang L, He Z. Bismuth impregnated biochar for efficient uranium removal from solution: Adsorption behavior and interfacial mechanism. Science of The Total Environment 2022c; 819: 153145.

Liatsou I, Michail G, Demetriou M, Pashalidis I. Uranium binding by biochar fibres derived from Luffa cylindrica after controlled surface oxidation. Journal of Radioanalytical and Nuclear Chemistry 2017; 311: 871-875.

Lin J, Dahan I, Valderrama B, Manuel MV. Structure and properties of uranium oxide thin films deposited by pulsed dc magnetron sputtering. Applied Surface Science 2014; 301: 475-480.

Lingamdinne LP, Choi JS, Angaru GKR, Karri RR, Yang JK, Chang YY, et al. Magnetic-watermelon rinds biochar for uranium-contaminated water treatment using an electromagnetic semi-batch column with removal mechanistic investigations. Chemosphere 2022; 286: 131776.

Liu W, Wang Q, Wang H, Xin Q, Hou W, Hu E, et al. Adsorption of uranium by chitosan/Chlorella pyrenoidosa composite adsorbent bearing phosphate ligand. Chemosphere 2022; 287: 132193.

Liu X, Ma R, Wang X, Ma Y, Yang Y, Zhuang L, et al. Graphene oxide-based materials for efficient removal of heavy metal ions from aqueous solution: A review. Environmental Pollution 2019; 252: 62-73.

Liu Y, Cao X, Hua R, Wang Y, Liu Y, Pang C, et al. Selective adsorption of uranyl ion on ion-imprinted chitosan/PVA cross-linked hydrogel. Hydrometallurgy 2010; 104: 150-155.

Liu Y, Liu Y, Cao X, Hua R, Wang Y, Pang C, et al. Biosorption studies of uranium (VI) on cross-linked chitosan: isotherm, kinetic and thermodynamic aspects. Journal of Radioanalytical and Nuclear Chemistry 2011; 290: 231-239.

Luo X, Zhang J, Tao J, Wang X, Zhao S, Chen Z, et al. Solar-powered “pump” for uranium recovery from seawater. Chemical Engineering Journal 2021; 416: 129486.

Michailidou G, Koumentakou I, Liakos EV, Lazaridou M, Lambropoulou DA, Bikiaris DN, et al. Adsorption of Uranium, Mercury, and Rare Earth Elements from Aqueous Solutions onto Magnetic Chitosan Adsorbents: A Review. Polymers 2021; 13: 3137.

Mishima K, Du X, Miyamoto N, Kano N, Imaizumi H. Experimental and Theoretical Studies on the Adsorption Mechanisms of Uranium (VI) Ions on Chitosan. Journal of Functional Biomaterials 2018; 9: 49.

Mishra V, Sureshkumar MK, Gupta N, Kaushik CP. Study on Sorption Characteristics of Uranium onto Biochar Derived from Eucalyptus Wood. Water, Air, & Soil Pollution 2017; 228: 309.

Morsy AMA. Adsorptive removal of uranium ions from liquid waste solutions by phosphorylated chitosan. Environmental Technology & Innovation 2015; 4: 299-310.

Mustafa J, Kausar A, Bhatti HN, Ilyas S. Sequestering of uranium (VI) onto eucalyptus bark: kinetic, equilibrium and thermodynamic studies. Desalination and Water Treatment 2016; 57: 14578-14589.

Neto CGT, Giacometti JA, Job AE, Ferreira FC, Fonseca JLC, Pereira MR. Thermal Analysis of Chitosan Based Networks. Carbohydrate Polymers 2005; 62: 97-103.

Noli F, Kapashi E, Kapnisti M. Biosorption of uranium and cadmium using sorbents based on Aloe vera wastes. Journal of Environmental Chemical Engineering 2019; 7: 102985.

Orabi AH, Abdelhamid AE, Salem HM, Ismaiel DA. Uranium removal using composite membranes incorporated with chitosan grafted phenylenediamine from liquid waste solution. Cellulose 2021; 28: 3703-3721.

Pan B, Pan B, Zhang W, Lv L, Zhang Q, Zheng S. Development of polymeric and polymer-based hybrid adsorbents for pollutants removal from waters. Chemical Engineering Journal 2009; 151: 19-29.

Pang C, Liu Y, Cao X, Hua R, Wang C, Li C. Adsorptive removal of uranium from aqueous solution using chitosan-coated attapulgite. Journal of Radioanalytical and Nuclear Chemistry 2010; 286: 185-193.

Patel H. Review on solvent desorption study from exhausted adsorbent. Journal of Saudi Chemical Society 2021; 25: 101302.

Philippou K, Anastopoulos I, Dosche C, Pashalidis I. Synthesis and characterization of a novel Fe3O4-loaded oxidized biochar from pine needles and its application for

uranium removal. Kinetic, thermodynamic, and mechanistic analysis. Journal of Environmental Management 2019; 252: 109677.

Repo E, Koivula R, Harjula R, Sillanpää M. Effect of EDTA and some other interfering species on the adsorption of Co(II) by EDTA-modified chitosan. Desalination 2013; 321: 93–102.

Repo E, Malinen L, Koivula R, Harjula R, Sillanpää M. Capture of Co(II) from its aqueous EDTA-chelate by DTPA-modified silica gel and chitosan. Journal of Hazardous Materials 2011a; 187: 122-132.

Repo E, Warchoł JK, Bhatnagar A, Sillanpää M. Heavy metals adsorption by novel EDTA-modified chitosan-silica hybrid materials. J Colloid Interface Sci 2011b; 358: 261-7.

Repo E, Warchol JK, Kurniawan TA, Sillanpää MET. Adsorption of Co(II) and Ni(II) by EDTA- and/or DTPA-modified chitosan: Kinetic and equilibrium modeling. Chemical Engineering Journal 2010; 161: 73-82.

Rostamian R, Firouzzare M, Irandoust M. Preparation and neutralization of forcespun chitosan nanofibers from shrimp shell waste and study on its uranium adsorption in aqueous media. Reactive and Functional Polymers 2019; 143: 104335.

Sadhu M, Bhattacharya P, Vithanage M, Padmaja Sudhakar P. Adsorptive removal of fluoride using biochar – A potential application in drinking water treatment. Separation and Purification Technology 2021; 278: 119106.

Saifuddin N, Dinara S. Immobilization of Saccharomyces cerevisiae onto cross-linked chitosan coated with magnetic nanoparticles for adsorption of uranium (VI) ions. Adv Nat Appl Sci 2012; 6: 249-267.

Sharma M, Chaudhary K, Kumari M, Yadav P, Sachdev K, Chandra Janu V, et al. Highly efficient, economic, and recyclable glutathione decorated magnetically separable nanocomposite for uranium(VI) adsorption from aqueous solution. Materials Today Chemistry 2020; 18: 100379.

Siddiqui SI, Singh PN, Tara N, Pal S, Chaudhry SA, Sinha I. Arsenic removal from water by starch functionalized maghemite nano-adsorbents: Thermodynamics and kinetics investigations. Colloid and Interface Science Communications 2020; 36: 100263.

Sureshkumar MK, Das D, Mallia MB, Gupta PC. Adsorption of uranium from aqueous solution using chitosan-tripolyphosphate (CTPP) beads. Journal of Hazardous Materials 2010; 184: 65-72.

Tran H, You S-J, Chao H-P. Effect of pyrolysis temperatures and times on the adsorption of cadmium onto orange peel derived biochar. Waste Management & Research 2015; 34.

Wang B, Zheng J, Li Y, Zaidi A, Hu Y, Hu B. Fabrication of δ-MnO2-modified algal biochar for efficient removal of U (VI) from aqueous solutions. Journal of Environmental Chemical Engineering 2021; 9: 105625.

Wang G, Liu J, Wang X, Xie Z, Deng N. Adsorption of uranium (VI) from aqueous solution onto cross-linked chitosan. Journal of Hazardous Materials 2009; 168: 1053-1058.

Wang J-s, Peng R-t, Yang J-h, Liu Y-c, Hu X-j. Preparation of ethylenediamine-modified magnetic chitosan complex for adsorption of uranyl ions. Carbohydrate Polymers 2011; 84: 1169-1175.

Wang J, Huo Y, Ai Y. Experimental and theoretical studies of chitosan modified titanium dioxide composites for uranium and europium removal. Cellulose 2020; 27: 7765-7777.

Wang S, Guo W, Gao F, Wang Y, Gao Y. Lead and uranium sorptive removal from aqueous solution using magnetic and nonmagnetic fast pyrolysis rice husk biochars. RSC advances 2018; 8: 13205-13217.

Wang X, Chen L, Wang L, Fan Q, Pan D, Li J, et al. Synthesis of novel nanomaterials and their application in efficient removal of radionuclides. Science China Chemistry 2019; 62: 933-967.

Wang Z, Wang Y, Yao C. Highly Efficient Removal of Uranium(VI) From Aqueous Solution Using the Polyethyleneimine Modified Magnetic Chitosan. Journal of Polymers and the Environment 2022; 30: 1-12.

Wu W, Yang M, Feng Q, McGrouther K, Wang H, Lu H, et al. Chemical characterization of rice straw-derived biochar for soil amendment. Biomass and Bioenergy 2012; 47: 268-276.

Xu J, Chen M, Zhang C, Yi Z. Adsorption of uranium(VI) from aqueous solution by diethylenetriamine-functionalized magnetic chitosan. Journal of Radioanalytical and Nuclear Chemistry 2013; 298: 1375-1383.

Xu Z, Xing Y, Ren A, Ma D, Li Y, Hu S. Study on adsorption properties of water hyacinth-derived biochar for uranium (VI). Journal of Radioanalytical and Nuclear Chemistry 2020; 324: 1317-1327.

Yakout SM. Effect of porosity and surface chemistry on the adsorption-desorption of uranium(VI) from aqueous solution and groundwater. Journal of Radioanalytical and Nuclear Chemistry 2016; 308: 555-565.

Yang L, Huang C, Luo X, Zhang L, Ye Y, Jun H, et al. Chitosan-based aerogel with anti-swelling for U(VI) adsorption from aqueous solution. Colloids and Surfaces A: Physicochemical and Engineering Aspects 2021; 630: 127527.

Yu S-l, Dai Y, Cao X-h, Zhang Z-b, Liu Y-h, Ma H-j, et al. Adsorption of uranium(VI) from aqueous solution using a novel magnetic hydrothermal cross-linking chitosan. Journal of Radioanalytical and Nuclear Chemistry 2016; 310: 651-660.

Zhao W, Hao C, Guo Y, Shao W, Tian Y, Zhao P. Optimization of Adsorption Conditions Using Response Surface Methodology for Tetracycline Removal by MnFe2O4/Multi-Wall Carbon Nanotubes. Water 2023; 15: 2392.

Zheng X, Wu J, Yan X, Qin G, Zhou R, Wei Z. Biochar-induced soil phosphate sorption and availability depend on soil properties: a microcosm study. Journal of Soils and Sediments 2020; 20: 1-11.

Zhou L, Jia Y, Peng J, Liu Z, Al-Zaini E. Competitive adsorption of uranium(VI) and thorium(IV) ions from aqueous solution using triphosphate-crosslinked magnetic chitosan resins. Journal of Radioanalytical and Nuclear Chemistry 2014; 302: 331-340.

Zhou L, Shang C, Liu Z, Huang G, Adesina AA. Selective adsorption of uranium(VI) from aqueous solutions using the ion-imprinted magnetic chitosan resins. Journal of Colloid and Interface Science 2012; 366: 165-172.

Zhou L, Zou H, Wang Y, Huang Z, Wang Y, Luo T, et al. Adsorption of uranium(VI) from aqueous solution using magnetic carboxymethyl chitosan nano-particles functionalized with ethylenediamine. Journal of Radioanalytical and Nuclear Chemistry 2016; 308: 935-946.

Zhuang S, Cheng R, Kang M, Wang J. Kinetic and equilibrium of U(VI) adsorption onto magnetic amidoxime-functionalized chitosan beads. Journal of Cleaner Production 2018; 188: 655-661.